Contents lists available at ScienceDirect

Applied Acoustics

journal homepage: www.elsevier.com/locate/apacoust

Efficient finite difference modeling of infrasound propagation in realistic 3D domains: Validation with wind turbine measurements

Ken Mattsson[a,b,*], Gustav Eriksson[a], Leif Persson[a], José Chilo[b], Kourosh Tatar[b]

[a] Uppsala University, Department of Information Technology, Uppsala, Sweden, Sweden
[b] University of Gävle, Gävle, Sweden, Sweden

HIGHLIGHTS

- 3D low-frequency simulation tool for complex domains.
- Validation against infrasound wind farm measurements.
- Verification against realistic 2D and 3D benchmark problems.
- Verification of long-propagation effects in different atmospheres.
- Determination of the infrasound sound power levels of modern wind-turbines.

ARTICLE INFO

Keywords:
Finite difference methods
Infrasound measurement
Infrasound simulations
Validation
Verification

ABSTRACT

We present a high-fidelity simulation tool for accurate acoustic modeling across a wide range of applications. The numerical method is based on diagonal-norm Summation-By-Parts (SBP) finite-difference operators, which guarantee linear stability on piecewise curvilinear multi-block grids. Realistic three-dimensional atmospheric and topographic data are directly incorporated into the simulations, and the solver is implemented in CUDA to achieve high computational efficiency. Verification is performed through convergence studies against highly resolved benchmark problems in both two and three spatial dimensions, while validation is carried out using high-quality infrasound measurements from two modern wind farms in Sweden. The results show that modern, large-scale wind turbines generate infrasound levels significantly higher than those reported for older, smaller turbines. These findings advance the understanding of the acoustic characteristics of contemporary wind turbines and provide important guidance for assessing their potential environmental and societal impacts.

1. Introduction

Silence has become a scarce commodity in modern society. Among environmental stressors, traffic noise is recognized as one of the most significant threats to public health [1,2]. Long-term exposure has been associated with an increased risk of cardiovascular disease [3], as well as annoyance, sleep disturbance, and impaired cognitive performance in children [4]. To mitigate such impacts, reliable and precise computational tools capable of predicting noise propagation and generating noise maps are essential. Such tools are indispensable for the planning of urban communities, transportation infrastructure, airports, and wind farms, as well as for safeguarding quiet areas in national parks and recreational environments.

Low-frequency noise (below 200 Hz) is of particular concern. It penetrates efficiently into and through buildings, and while the human auditory system spans 16 Hz - 18 kHz (often rounded to 20 Hz - 20 kHz) [5], frequencies below approximately 100 Hz are typically perceived as vibrations or pressure rather than tonal sound. Prominent outdoor sources include road, air, and rail traffic, construction activity, and modern wind turbines, while indoor contributions arise from heating, ventilation, air-conditioning systems, and industrial machinery. The combined influence of multiple sources can elevate exposure to levels sufficient to induce adverse health outcomes. Ensuring quiet residential conditions, particularly in sleeping environments, is therefore of critical importance.

---

* Corresponding author at: Uppsala University, Department of Information Technology, Uppsala, Sweden, Sweden.
Email addresses: ken.mattsson@it.uu.se (K. Mattsson), gustav.eriksson@it.uu.se (G. Eriksson), leif.persson@it.uu.se (L. Persson), Jose.Chilo@hig.se (J. Chilo), Kourosh.Tatar@hig.se (K. Tatar).

https://doi.org/10.1016/j.apacoust.2025.111156
Received 14 February 2025; Received in revised form 31 October 2025; Accepted 1 November 2025

Please cite this article as: Mattsson K, Eriksson G, Persson L, Chilo J, Tatar K. Efficient finite difference modeling of infrasound propagation in realistic 3D domains: Validation with wind turbine measurements. Applied Acoustics. doi: https://doi.org/10.1016/j.apacoust.2025.111156.

Existing numerical methods for outdoor sound propagation have been shown to be inadequate for large-scale domains with complex and irregular terrain [6]. More accurate and advanced computational approaches have recently been developed to address these shortcomings [7]. Empirical measurements further confirm [8,9] that accurate prediction of sound pressure levels (SPL) over extended ranges requires explicit consideration of both the three-dimensional atmospheric state and the underlying terrain. The dynamic atmosphere influences acoustic propagation across all ranges, but its spatiotemporal variability becomes increasingly significant with distance. Consequently, high-fidelity simulations of long-range sound propagation (typically exceeding 500 m) must incorporate: 1) atmospheric attenuation, 2) wind effects, 3) altitude-dependent sound speed, 4) stratification and buoyancy, 5) irregular terrain, and 6) realistic boundary conditions.

Sound propagation in a heterogeneous atmosphere is modeled in this study using the three-dimensional acoustic wave equation [10]. To guarantee stability and convergence, diagonal-norm SBP finite-difference operators are combined with the Simultaneous Approximation Term (SAT) technique for the weak enforcement of boundary conditions. Over the past two decades, the SBP-SAT framework has been extensively developed and rigorously analyzed, and it has consistently been shown to provide highly accurate and reliable numerical simulations of acoustic wave propagation (see, e.g., [6,7,11–16]).

For a computational tool to be broadly useful to the scientific and engineering community, it must satisfy three essential criteria: 1) the methodology must be rigorously validated and transparently documented; 2) the results must be clear, interpretable, and visually accessible; and 3) the tool must be user-friendly, avoiding the need for tuning of ad hoc parameters. To achieve all of this is the overarching goal of the sound simulation tool named *SoundSim360*. In contrast, widely used commercial noise simulation software, including models such as Nord2000, are based on ray-tracing techniques that require numerous adjustable parameters. While such models are computationally efficient, they exhibit several well-known limitations that we avoid by directly solving the full three-dimensional acoustic wave equation. Four key weaknesses of ray-tracing approaches are: 1) inadequate treatment of low-frequency sound (below 200 Hz), 2) difficulty in handling complex geometries, 3) limited capability to model sound transmission through walls, and 4) inability to accurately capture transient sources.

As an illustrative example, Fig. 1 presents a comparison between SoundSim360 and Nord2000 (as implemented in the commercial software SoundPlan 9.1) for a 25 Hz monopole source located at Polacksbacken, Uppsala University. The source is positioned 10 m above ground with a sound power level of 105 dB. Terrain and building data are obtained from Lantmäteriet [17], and the ground is modeled as a hard surface (impedance class H in Nord2000). All other Nord2000 parameters are kept at their default values. The sound pressure level (SPL) distribution at 2 m height is shown for both models. The computational domain for SoundSim360 covers 500 m × 600 m × 250 m.

Significant discrepancies occur in the acoustic shadow zones behind buildings, where Nord2000 systematically underestimates SPL due to fundamental limitations of ray-based propagation at low frequencies. The model cannot accurately simulate edge diffraction at these frequencies, as it relies on geometrical acoustics and is calibrated for higher-frequency sound. At longer wavelengths, these assumptions break down, and wave-based diffraction effects dominate the propagation field.

Infrasound refers to sound waves with frequencies below 20 Hz and is produced by various natural and man-made sources. Examples of man-made infrasound sources include explosions, engines, ventilation, high-speed trains, high-speed aircraft, rockets, and wind turbines. Natural sources of infrasound are diverse: volcanic eruptions, auroras, lightning and sprites, surf, wave-wave ocean interactions (microbaroms), avalanches, meteors, mountain-associated waves, earthquakes, and tsunamis.

Infrasound simulations are increasingly employed in geophysical research and monitoring for a variety of applications. These simulations help scientists study the behavior of infrasound waves in different environments and understand their implications in various geophysical contexts. Here are a few key geophysical applications where infrasound simulations are used: 1) to detect large explosions (including nuclear tests) [18,19], 2) to detect natural disasters like, earthquakes [20,21], tsunamis or volcanic eruptions [22], 3) to provide data on atmospheric conditions [23–25] and to improve forecasting models. These applications typically require the combination of accurate infrasound (and sometimes seismic) measurements and advanced numerical methods to simulate infrasound propagation in the atmosphere up to 140 km. A popular numerical method for infrasound simulations in a relatively flat terrain, with a single source, is the wide angle parabolic equation method [18,20,24,25]. To capture interference from multiple sources in irregular terrain, a three-dimensional wave equation model is necessary.

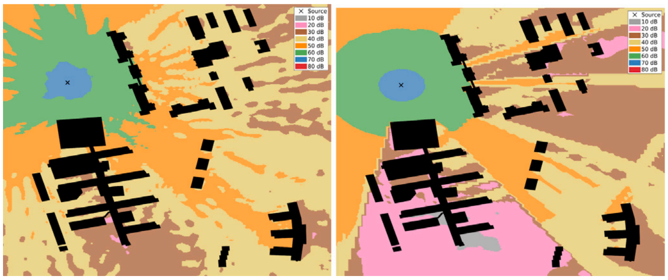

(a) SoundSim360 (b) Nord2000

Fig. 1. Low-frequency (25 Hz) sound simulation at polacksbacken (105 dB point source at ×, 10 m above ground), comparing (a) SoundSim360 and (b) Nord2000. Shown are sound pressure levels 2 m above ground. Nord2000 cannot accurately model edge diffraction at low frequencies, where long wavelengths cause pronounced wave bending around obstacles.

The main focus of the present study is twofold. The first main focus is to validate the simulation tool against accurate infrasound measurements. Infrasound is an ideal candidate to validate an outdoor sound simulation tool due to the minimal atmospheric (and ground) damping allowing for long-distance propagation. Modern wind turbines are strong infrasound emitters and are often located remotely, far away from cities and highways that would otherwise contribute to relatively high background noise. The second main focus is to map the sound power levels in the infrasound regime for a few modern types of wind turbines and examine the influence of the atmosphere. We have carried out measurements at Målarberget wind farm three times: 2023–10-26, 2024–10-23, and 2024–12-16, and at Lervik wind farm twice: 2024–05-21 and 2024–09-10.

After these initial infrasound measurements, two of us experienced sleep disorders and migraine headaches. These symptoms appeared after being exposed to infrasound levels of just over 95 dB around the 1 Hz frequency band for at least 4 hours (see Fig. 7). Similar symptoms during infrasound measurements have been reported in [26]. It is well-known among specialists in otoneurology and otolaryngology that inaudible infrasound has the potential to trigger migraines in people with a more sensitive nervous system, for example, see [27–29]. One in three people is predisposed to migraines, with a more sensitive nervous system [30,31]. The level of sensitivity is highly individual. There are new studies that link the impact of inaudible infrasound to brain activity [32,33]. As early as 1985, Danielsson and Landström [34] showed that infrasound at levels of 95 dB during 1 h of exposure causes an increase in diastolic blood pressure and decreases in systolic blood pressure and pulse rate. More recent studies also show that many animals move more than 5 km from wind turbines, especially deer and birds [35].

Other (recent) studies [36,37] suggest that infrasound from wind turbines does not produce measurable health effects. In [37], 27 participants were exposed to 89 dB of infrasound for 10 min in a laboratory, while in [36], 37 participants were exposed to 87 dB for three days. These studies have certain limitations: they did not involve experts in otoneurology or otolaryngology in their design, and participants with known sensitivities, such as individuals prone to migraines, were not included. Furthermore, the short-term laboratory exposures may not fully reflect long-term, cumulative exposure in residential environments near wind farms. Consequently, while informative, the results should be interpreted with caution, particularly when considering potential effects on sensitive subpopulations.

It is well-known [38,39] that repetitive, pulsating sounds are perceived as more disturbing than continuous sounds with the same frequency content and average sound level. Each time a wind turbine blade passes the tower, a pressure pulse with steep edges is generated, which propagates as infrasound. The blade passage frequency (BPF) can be determined by counting the number of blade passes per minute and dividing by 60. The BPF decreases with increasing turbine blade size, and larger blades also produce stronger pressure pulses, resulting in more intense infrasound. For modern wind turbines, the BPF typically ranges between 0.2 and 0.5 Hz, whereas older turbines exhibit a higher BPF of around 0.7 to 0.9 Hz. In sound pressure spectra, the BPF and its harmonics (multiples of the BPF) appear as distinct spikes [26,40]. This pattern contrasts sharply with natural infrasound, which is typically broadband generated by meteorological events, and lacks such discrete spikes. Based on this, it is reasonable to hypothesize that humans are generally unaffected by natural infrasound. However, the unnatural characteristics of wind turbine infrasound, arising from its repetitive pulses, may contribute to the symptoms reported in the vicinity of wind turbines.

The health impacts of wind turbine infrasound remain unresolved, largely due to limitations in existing laboratory studies. To date, no controlled experiment has accurately reproduced the characteristic pulsating infrasound emitted by modern turbines. Instead, previous studies have relied on continuous broadband infrasound at comparatively modest levels [36,37]. These conditions do not reflect real-world exposure. A scientifically robust study must therefore include a realistic reproduction of pulsating infrasound, exposure periods lasting several weeks, a sufficiently large and diverse group of participants–including individuals with known sensitivities such as migraines–and the involvement of medical experts in otoneurology and otolaryngology. Until such studies are conducted, it is premature to draw definitive conclusions regarding the health effects of wind turbine infrasound.

The remainder of this paper is organized as follows. In Section 2, we introduce the acoustic wave equation model and establish its well-posedness, including a discussion of various boundary conditions and the model data. Section 3 presents the spatial discretization and the explicit second-order time integration scheme. A brief account of the implementation is given in Section 4. The accuracy of the method is verified against 2D and 3D benchmark problems in Section 5. In Section 6, we describe infrasound measurements from two different wind farms, and in Section 7 we validate the simulations against these measurements and present results on infrasound propagation around the wind farms. Finally, Section 8 summarizes the main findings of this work.

2. The physical model

The model we use for sound propagation is the 3D acoustic wave equation in second-order form [10], given by

$$\frac{1}{c(\boldsymbol{x})^2\rho(\boldsymbol{x})}u_{tt} = \nabla\cdot\left(\frac{1}{\rho(\boldsymbol{x})}\nabla u\right) + \beta(\boldsymbol{x})u_t + \frac{1}{c(\boldsymbol{x})^2\rho(\boldsymbol{x})}S(\boldsymbol{x},t), \quad \boldsymbol{x}\in\Omega, \quad t>0\,, \tag{1}$$

where $u = u(\boldsymbol{x}, t)$ is the pressure deviation, $c(\boldsymbol{x})$ is the speed of sound, $\rho(\boldsymbol{x})$ is the density of the medium, $\beta(\boldsymbol{x})$ is a damping coefficient, $S(\boldsymbol{x}, t)$ is a forcing function, and $\Omega \subset \mathbb{R}^3$ is the computational domain. Here $\boldsymbol{x} \in \Omega$ is the 3D spatial coordinate and t is the time coordinate. Throughout the paper we use bold font to denote vectors. In (1) subscripts are used to denote partial differentiation. In this work the computational domain Ω is a box with a variable bottom boundary to take into account the ground elevation. We denote the boundary of Ω as $\partial\Omega$.

To obtain unique solutions to (1) we have to impose initial and boundary conditions on the solution $u(\boldsymbol{x}, t)$. In this work, we exclusively use homogeneous initial conditions, i.e., $u(\boldsymbol{x}, 0) = u_t(\boldsymbol{x}, 0) = 0$. We split the boundary into two parts, $\partial\Omega_g$ on the ground and $\partial\Omega_o$ elsewhere, and impose the following boundary conditions:

$$\begin{aligned} &\text{First-order outflow:} && c(\boldsymbol{x})\boldsymbol{n}\cdot\nabla u + u_t = 0, && \boldsymbol{x}\in\partial\Omega_o,\\ &\text{Impedance:} && p(\boldsymbol{x})\omega u + c(\boldsymbol{x})\boldsymbol{n}\cdot\nabla u + q(\boldsymbol{x})u_t = 0, && \boldsymbol{x}\in\partial\Omega_g, \end{aligned} \tag{2}$$

where $\boldsymbol{n}$ denotes the outgoing normal. The first-order outflow boundary condition on $\partial\Omega_o$ is used to truncate the domain and minimize reflections at artificial boundaries. The impedance boundary condition on $\partial\Omega_g$ is taken from [41], and is used for partially reflecting surfaces (such as the ground). The parameters $p(\boldsymbol{x})$ and $q(\boldsymbol{x})$ are defined by $p(\boldsymbol{x})+q(\boldsymbol{x})i = \frac{i}{\hat{Z}(\boldsymbol{x})}$, where $\hat{Z}(\boldsymbol{x})$ is the normalized surface impedance. Here we use a formula from [42] that is valid for low frequencies, given by

$$\hat{Z}(\boldsymbol{x}) = \sqrt{\frac{\sigma_e(\boldsymbol{x})}{2\omega\gamma\rho(\boldsymbol{x})}}(1+i), \quad \boldsymbol{x}\in\partial\Omega_g\,, \tag{3}$$

where $\sigma_e(\boldsymbol{x})$ is the effective flow resistivity of the ground surface, $\gamma = 1.4$ is the specific heat ratio, and $\omega = 2\pi f$ with f being the frequency.

In the present study, the forcing function consists of a single point source, i.e.,

$$S(\boldsymbol{x}, t) = \delta(\boldsymbol{x} - \boldsymbol{x}^*)g(t), \tag{4}$$

where δ is the Dirac delta function, $\boldsymbol{x}^*$ is the location of point source, and $g(t)$ is the time signal. Here we use ramped harmonic signals of the form

$$g(t) = Ar(t)\sin(\omega t), \tag{5}$$

where A is the amplitude and $r(t)$ is a ramping function given by

$$r(t) = \begin{cases} \sin^2\left(\frac{\pi t}{2T_{\text{ramp}}}\right), & 0 \le t < T_{\text{ramp}},\\ 1 & t \ge T_{\text{ramp}}, \end{cases} \tag{6}$$

with $T_{\text{ramp}} = \frac{6}{f}$ (six periods ramping). To model problems with multiple sources, for example a wind farm, we solve (1) with one source at a time and combine the results. As we shall see later, this is necessary to properly incorporate wind effects into the model. Note that we do not include any phase information in the time-signal (5). This is because the phases of the sources we consider here (wind turbines) are generally unknown, and by solving (1) with one source at a time we can reconstruct all possible phase combinations a posteriori regardless.

2.1. Sound pressure level computation

Consider a simulation with all sources active at the same time (with independent, random phases). Let $P(\boldsymbol{x})$ denote the random variable corresponding to the total mean-square pressure at receiver position $\boldsymbol{x}$, and let

$$L(\boldsymbol{x}) = 10\log_{10}\left(\frac{P(\boldsymbol{x})}{p_0^2}\right),$$

be the corresponding sound pressure level (SPL) relative to the reference pressure $p_0 = 20\ \mu$Pa. Depending on the specific realization of phases, the SPL will vary significantly. In this paper we disregard this variation, i.e., we ignore the effects of phases altogether, by considering only the expected SPL over all possible phase combinations, which we compute from the individual simulations with one source at a time. Let $(p_{i,\text{rms}}(\boldsymbol{x}))^2$,

$i = 1, 2, \ldots, N_s$, be the mean-square RMS pressure (with one point source located in $\boldsymbol{x}_i^*$) sampled over ten periods as follows:

$$(p_{i,\mathrm{rms}}(\boldsymbol{x}))^2 = \frac{f}{10}\int_{t^*}^{t^*+\frac{10}{f}} \left(u(\boldsymbol{x}, t; \boldsymbol{x}_i^*)\right)^2 dt, \quad i = 1, 2, \ldots, N_s. \tag{7}$$

Here $u(\boldsymbol{x}, t; \boldsymbol{x}_i^*)$ is the solution with the point source located in $\boldsymbol{x}_i^*$, and N_s is the total number of sources. We start sampling at

$$t^* = T_{\mathrm{ramp}} + \frac{\sup_{\boldsymbol{x}\in\Omega} |\boldsymbol{x} - \boldsymbol{x}^*|}{\inf_{\boldsymbol{x}\in\Omega} c(\boldsymbol{x})}, \tag{8}$$

which is sufficiently large to ensure that $u(\boldsymbol{x}, t; \boldsymbol{x}_i^*)$ is harmonic at all points in space when $t > t^*$. It can be shown (derivation omitted) that

$$\mathbb{E}[P(\boldsymbol{x})] = \sum_{i=1}^{N_s} (p_{i,\mathrm{rms}}(\boldsymbol{x}))^2, \tag{9}$$

i.e., the expected total mean-square pressure is just the sum of the mean-square pressure when simulating with one source at a time. This is intuitive, since the probabilities of constructive and destructive interference balance on average, so the expected level is simply the sum of the individual mean-square contributions without interaction terms. We define the expected SPL as

$$L_{\mathrm{tot}}(\boldsymbol{x}) = 10\log_{10}\left(\frac{\mathbb{E}[P(\boldsymbol{x})]}{p_0^2}\right) = 10\log_{10}\left(\frac{\sum_{i=1}^{N_s} (p_{i,\mathrm{rms}}(\boldsymbol{x}))^2}{p_0^2}\right). \tag{10}$$

Note that $L_{\mathrm{tot}}(\boldsymbol{x})$ is not the same as $\mathbb{E}[L(\boldsymbol{x})]$. The former is defined from the expected mean-square pressure and corresponds to the conventional way of reporting average SPL from incoherent sources, whereas $\mathbb{E}[L(\boldsymbol{x})]$ is the strict statistical mean of the random decibel values. In the case where the sources contribute with comparable strength, $\mathbb{E}[L(\boldsymbol{x})] \approx L_{\mathrm{tot}}(\boldsymbol{x}) - 2.5$ dB.

The spread of $L(\boldsymbol{x})$ around its mean depends on how unevenly the sources contribute at the receiver position $\boldsymbol{x}$. When many sources contribute with comparable strength (for example, far from the wind farm) and their phases are independent and uniformly distributed, $P(\boldsymbol{x})$ is approximately exponentially distributed. In this case the distribution of $L(\boldsymbol{x})$ has a standard deviation

$$\mathrm{sd}(L(\boldsymbol{x})) = \frac{10}{\ln 10}\sqrt{\frac{\pi^2}{6}} \approx 5.57 \text{ dB}, \tag{11}$$

independent of the mean. If one or a few sources dominate, for example very close to a wind turbine, the distribution departs from exponential and the spread of $L(\boldsymbol{x})$ is significantly smaller. In particular, in the immediate vicinity of a turbine the SPL will be almost entirely determined by that single source, and the phases of the other turbines become irrelevant. Hence, inside the wind farm and near individual turbines, the standard deviation $\mathrm{sd}(L(\boldsymbol{x}))$ is close to zero.

Remark 1. Later in the paper we compare the expected SPL values $L_{\mathrm{tot}}(\boldsymbol{x})$ from simulations to measurements from real wind farms. One could argue that the measurement is done with a specific phase combination, and therefore we should try to find that combination in the simulations as well. However, we argue that any specific interference pattern will be highly affected by temporal variations in the sources and atmospheric parameters, which are diminished since the measurements take place over several minutes. We emphasize that the simulation results we present are not snapshots of the SPL at any given time, rather they should be viewed as averages over all possible phase combinations under the assumptions of our model. In reality, local variations of the SPL in both time and space will be significant.

2.2. *Wind modeling*

The effect of wind is modeled by replacing $c(\boldsymbol{x})$ and $\rho(\boldsymbol{x})$ in (1) with the *effective speed of sound* and the *effective density* [43], defined as

$$c_{\mathrm{eff}}(\boldsymbol{x}) = c(\boldsymbol{x}) + \hat{\mathbf{s}}(\boldsymbol{x}) \cdot \mathbf{V}(\boldsymbol{x}) \quad \text{and} \quad \rho_{\mathrm{eff}}(\boldsymbol{x}) = \rho(\boldsymbol{x}) - \frac{2\rho_0}{c_0}\hat{\mathbf{s}}(\boldsymbol{x}) \cdot \mathbf{V}(\boldsymbol{x}), \tag{12}$$

where $\hat{\mathbf{s}}(\boldsymbol{x}) = \frac{\boldsymbol{x}-\boldsymbol{x}^*}{|\boldsymbol{x}-\boldsymbol{x}^*|}$ is the unit vector in the sound propagation direction, $\mathbf{V}(\boldsymbol{x})$ is the wind vector, and $c_0 = 340.3$ m/s and $\rho_0 = 1.225$ kg/m^3 are atmospheric reference values. This approximation is valid when most of the sound propagates along $\hat{\mathbf{s}}(\boldsymbol{x})$, which is true if we solve for one source at a time and if both the source and the receiver are located close to the ground [9,44].

Remark 2. The approximation in [43] is valid under the assumptions that variations in density and speed of sound remain moderate, and that the wind speed is much smaller than the speed of sound. These conditions are satisfied for the problems considered in the present study. For a more general and accurate treatment of 3D time-dependent wind effects, one must instead employ the linearized Euler equations in 3D, as demonstrated in [7,45].

2.3. *Model data*

To obtain useful and trustworthy results from simulations it is crucial to use real-world data. In our model, the coefficients we need to specify are the speed of sound $c(\boldsymbol{x})$, the density $\rho(\boldsymbol{x})$, the attenuation $\beta(\boldsymbol{x})$, the wind $\mathbf{V}(\boldsymbol{x})$, the effective flow resistivity $\sigma_e(\boldsymbol{x})$, and the source position $\boldsymbol{x}^*$ and amplitude A. We use elevation data provided by *Lantmäteriet* [17] (1 m resolution) to construct Ω. The upper limit is set at 5 km for all simulations.

For large-scale outdoor simulations, it is particularly important to incorporate atmospheric data into the model. In the present study, we use MEPS atmospheric data from *The Norwegian Meteorological Institute*, which provides all the atmospheric data we need with one hour temporal resolution and 2.5 km spatial resolution with 65 height levels up to approximately 10 km. The atmospheric attenuation (damping) coefficient is defined as a function of temperature, pressure, humidity, and frequency [46]. The speed of sound and density are computed from the temperature, pressure, and humidity data according to the formulas presented in [47].

The effective flow resistivity σ_e for the ground boundary condition is highly dependent on the type of ground surface in the computational domain. In this work we distinguish between two different types, hard and semi-hard. We use land cover data from Naturvårdsverket [48], which categorizes the entire surface of Sweden into several ground classes. We set $\sigma_e = 200{,}000{,}000$ Pa $\cdot$ s/m^2 for obviously hard surfaces (water, asphalt etc.) and $\sigma_e = 500{,}000$ Pa $\cdot$ s/m^2 for the rest (forest floor, farming fields etc.). These choices are fairly conservative, possibly resulting in too low ground attenuation. But investigating the uncertainties involved in modeling the ground boundary solely based on data available from satellite imagery and airplane laser scanning is beyond the scope of this study.

We model the wind turbine in each simulation as a point source located at the hub. The coordinates of each turbine and its hub height are obtained from the original sound emission calculations (the basis for the permit application of the wind farm).

In the present paper we focus on sound propagation for the frequency $f = 1$ Hz, which is the lowest frequency we can measure with the current equipment. Ideally, the infrasound measurements should go down to 0.1 Hz to capture the BPF from the new larger wind turbines, expected to be between 0.2–0.5 Hz. We will use measurements on real wind farms to determine the source amplitudes A at 1 Hz, so that the measured SPL values match the simulated SPL values as well as possible. The sound power levels we report should be understood in the context of our sound propagation model, which is a simplification of reality. First, we make the assumption that all turbines are point sources located in the hub (no directivity) and that they all emit the same sound power. The second major uncertainty is the atmospheric and ground data, which have a limited resolution and accuracy. However, as we show in Section 7.3, the influence of the atmosphere is relatively small at the distances where we perform the measurements. A more detailed analysis of the directivity of wind turbines in the infrasound region and the amount of uncertainty from the atmospheric data is out of scope in the present study.

Remark 3. By combining accurate sound measurements, current atmospheric data, and our simulation tool, the sound power levels of the sources can be determined across the entire low-frequency range (under the assumptions of our model). High-frequency sound can also be analyzed with this technique, but would naturally be confined to much smaller domains, due to the large atmospheric and ground absorption.

2.4. Energy method

For linear problems, the energy method can be used to prove stability of PDEs, and hence it is important for well-posedness [49]. Let

$$(u,v)_{\Omega} = \int_{\Omega} uv\, d\boldsymbol{x} \quad \text{and} \quad (u,v)_{\partial\Omega} = \int_{\partial\Omega} uv\, d\boldsymbol{x} \quad \forall u,v \in \mathbb{R}, \tag{13}$$

denote L^2-inner products over the domain and its boundary, respectively.

To simplify the upcoming analysis we collect terms and write the PDE as

$$\begin{aligned} &u_{tt} = a\nabla\cdot(b\nabla u) + \alpha u_t + S(\boldsymbol{x},t), && x\in\Omega, \quad t>0 \\ &\gamma_1\, u + b\boldsymbol{n}\cdot\nabla u + \gamma_2 u_t = 0, && x\in\partial\Omega,\ t>0, \\ &u = u_t = 0, && x\in\Omega, \quad t=0, \end{aligned} \tag{14}$$

where $a = a(\boldsymbol{x}) = c(\boldsymbol{x})^2\rho(\boldsymbol{x})$, $b = b(\boldsymbol{x}) = \frac{1}{\rho(\boldsymbol{x})}$, $\alpha = \alpha(\boldsymbol{x}) = \beta(\boldsymbol{x})c(\boldsymbol{x})^2\rho(\boldsymbol{x})$, and $\gamma_1 = \gamma_1(\boldsymbol{x})$ and $\gamma_2 = \gamma_2(\boldsymbol{x})$ determine the boundary condition. With this general boundary condition, we can treat both first-order outflow boundary conditions ($\gamma_1 = 0$ and $\gamma_2 = \frac{b(\boldsymbol{x})}{c(\boldsymbol{x})}$) and impedance boundary conditions ($\gamma_1 = \frac{b(\boldsymbol{x})p\omega}{c(\boldsymbol{x})}$ and $\gamma_2 = \frac{b(\boldsymbol{x})}{c(\boldsymbol{x})}q$). In (14) we have also included the homogeneous initial conditions.

Source data does not influence stability [49], hence we set $S(t) = 0$ in the following stability analysis. Multiplying the PDE (14) by u_t and integrating over the domain Ω gives

$$\begin{aligned} \left(u_t, \frac{1}{a}u_{tt}\right)_{\Omega} &= (u_t, \nabla\cdot(b\nabla u))_{\Omega} + (u_t, \beta u_t)_{\Omega} \\ &= -(\nabla u_t, b\nabla u)_{\Omega} + (u_t, b\boldsymbol{n}\cdot\nabla u)_{\partial\Omega} + (u_t, \beta u_t)_{\Omega} \\ &= -(\nabla u_t, b\nabla u)_{\Omega} - (u_t, \gamma_1\, u)_{\partial\Omega} - (u_t, \gamma_2 u_t)_{\partial\Omega} + (u_t, \beta u_t)_{\Omega}, \end{aligned} \tag{15}$$

where the boundary condition has been substituted in the last step. Rearranging terms leads to

$$\frac{d}{dt}E = -2(u_t, \gamma_2 u_t)_{\partial\Omega} + 2(u_t, \beta u_t)_{\Omega}, \tag{16}$$

where E is an energy given by

$$E = \left(u_t, \frac{1}{a}u_t\right)_{\Omega} + (\nabla u, b\nabla u)_{\Omega} + (u, \gamma_1\, u)_{\partial\Omega}. \tag{17}$$

For E to be a valid mathematical energy it must be non-negative, which is guaranteed if $a > 0$, $b \geq 0$, and $\gamma_1 \geq 0$. Stability is obtained if the energy is non-growing, i.e., if the right-hand side of (16) is non-positive, which is guaranteed if $\gamma_2 \geq 0$ and $\beta \leq 0$. These conditions are all fulfilled for the physical parameters used in our model. For linear PDEs, stability in combination with the correct number of boundary conditions is a sufficient condition for well-posedness [49].

Remark 4. The source term plays a crucial role in the model, although it does not influence stability or well-posedness, for which it is usually assumed to be zero. In the simulations, we retain a nonzero $S(t)$.

3. Discrete model

To retain space, we omit details on the spatial discretization. In short, we first compute a coordinate transformation of the domain Ω to a unit cube reference domain using linear transfinite interpolation. Then, we discretize the reference domain into an equidistant Cartesian grid and approximate all spatial operators using the well-documented SBP-SAT finite difference method. For details, we refer to [6,7,14–16,50–52]. For the wind farm simulations, we use second-order diagonal-norm SBP finite difference operators (derived in [15]) and sufficiently many grid points to obtain 10 points per wavelength relative to a wave speed of 330 m/s, in all directions.

The SBP-SAT method leads to a provably stable second-order ODE system given by,

$$\begin{aligned} &\boldsymbol{v}_{tt} = \boldsymbol{D}\boldsymbol{v} + \boldsymbol{E}\boldsymbol{v}_t + \boldsymbol{F}(t), && t>0, \\ &\boldsymbol{v}(0) = \boldsymbol{v}_t(0) = 0, && t=0, \end{aligned} \tag{18}$$

where $\boldsymbol{v} \in \mathbb{R}^N$ is the semi-discrete solution vector (time-dependent), N is the total number of grid points, $\boldsymbol{D}$ and $\boldsymbol{E}$ are negative semi-definite $N{\times}N$ matrices, and $\boldsymbol{F}(t)$ is the discretized forcing function (see [7,16,51] for details). In the present study, we utilize second, fourth, and sixth-order accurate diagonal-norm SBP finite difference operators, described in [15].

Remark 5. In [53] it was shown that a stable approximation of the wave equation in second-order form, using diagonal-norm SBP finite difference operators of second-, and fourth-order accuracy, yields convergence rates of order 2 and 4, respectively. This is verified in Table 1.

3.1. Temporal discretization

For time-stepping we use the following second-order explicit two-step method:

$$\frac{\boldsymbol{w}_{n+1} - 2\boldsymbol{w}_n + \boldsymbol{w}_{n-1}}{h^2} = \boldsymbol{D}\boldsymbol{w}_n + \boldsymbol{E}\frac{\boldsymbol{w}_{n+1} - \boldsymbol{w}_{n-1}}{2h} + \boldsymbol{F}(t_n), \quad n = 1,2,\ldots, \tag{19}$$

where h is a constant temporal step size, $t_n = hn$, $n = 0,1,2,\ldots$, and $\boldsymbol{w}_n$ is an approximation of $\boldsymbol{v}(t_n)$. Written as an iterative formula, we get

$$\left(\boldsymbol{I}_N - \frac{h}{2}\boldsymbol{E}\right)\boldsymbol{w}_{n+1} = (2\boldsymbol{I}_N + h^2\boldsymbol{D})\boldsymbol{w}_n - \left(\boldsymbol{I}_N + \frac{h}{2}\boldsymbol{E}\right)\boldsymbol{w}_{n-1} + h^2\boldsymbol{F}(t_n), \tag{20}$$

where $\boldsymbol{I}_N$ is the $N \times N$ temporal step size, that, due and the is an approximation of used, the matrix $\boldsymbol{E}$ is diagonal and hence $\left(\boldsymbol{I}_N - \frac{h}{2}\boldsymbol{E}\right)$ is easy to invert.

To retain second-order accuracy for all time we need to compute the initial time steps with second-order accuracy as well. The first time level is given by the initial data, i.e., $\boldsymbol{w}_0 = \boldsymbol{v}(0)$, but the second time level requires some more careful consideration, here we use the modified difference approach. Consider the first order approximation of the first derivative and its truncation error

$$\frac{\boldsymbol{v}(t_{n+1}) - \boldsymbol{v}(t_n)}{h} = \boldsymbol{v}_t(t_n) + \frac{h}{2}\boldsymbol{v}_{tt}(t_n) + \mathcal{O}(h^2). \tag{21}$$

Using the ODE (18) to substitute the term $\boldsymbol{v}_{tt}(t_n)$ we get

$$\frac{\boldsymbol{v}(t_{n+1}) - \boldsymbol{v}(t_n)}{h} = \boldsymbol{v}_t(t_n) + \frac{h}{2}(\boldsymbol{D}\boldsymbol{v}(t_n) + \boldsymbol{E}\boldsymbol{v}_t(t_n) + \boldsymbol{F}(t_n)) + \mathcal{O}(h^2). \tag{22}$$

which we use to compute a second-order accurate approximation of the solution at t_1, as follows:

$$\boldsymbol{w}_1 = \boldsymbol{v}(0) + h\boldsymbol{v}_t(0) + \frac{h^2}{2}(\boldsymbol{D}\boldsymbol{v}(0) + \boldsymbol{E}\boldsymbol{v}_t(0) + \boldsymbol{F}(0)). \tag{23}$$

With homogeneous initial data, we have $\boldsymbol{w}_0 = 0$ and $\boldsymbol{w}_1 = \frac{h^2}{2}\boldsymbol{F}(0)$.

The stability limit of the time-stepping formula (20) can be shown to be proportional to the smallest distance between two adjacent grid points. In this work, we determine the stability limit experimentally and, unless specified otherwise, choose the time step to be 50 % of the stability limit.

4. Implementation details

The numerical method is implemented in a custom code using C++ and CUDA for GPU acceleration. All pre- and postprocessing are done in Matlab (grid generation, reading data, constructing coefficient vectors, plotting etc.). We call the whole software package SoundSim360.

The simulations presented in this paper are performed on a single Nvidia RTX A6000 GPU, with 48 GB of internal memory and 10,752 CUDA cores. All simulations are done in single precision (the results with double precision are identical). The implementation is done in a matrix-free fashion, which means that only a handful of copies of the solution vectors have to be stored in memory (the spatially dependent coefficient and time-stepping vectors). As a reference for the performance of the GPU implementation, generating a noise map over a $15 \times 15 \times 5\,\mathrm{km}^3$ area, such as in Fig. 12, requires roughly 12 min of computation (24 simulations—one per source—at about 30 s each). A Matlab code using sparse matrices on a standard CPU would take roughly 20 hours to produce these results. In general, the Matlab implementation takes between 70 and 100 times longer compared to the GPU implementation, depending on the specific problem. Also, the matrix-based implementation utilizes significantly more memory and requires more preprocessing to assemble the matrices.

5. Verification

Before we turn to simulations with real-world data, we verify the accuracy and implementation of the numerical method by performing two verification tests. First, a comparison against a well-known benchmark problem and then a convergence study with physically relevant data.

5.1. Benchmark

We consider two of the 10 Hz benchmark problems presented in [54], referred to as Case 2 and Case 4. These problems consist of a single harmonic point source at $z = 5$ m, a flat topography, and a non-constant speed of sound profile. For Case 2 the speed of sound profile is defined as

$$c(z) = c_0 + 0.1z, \tag{24}$$

where $c_0 = 343$ m/s and $z \geq 0$. This profile gives rise to significant downward refraction on all heights. The Case 4 profile is defined as

$$c'(z) = \begin{cases} 0.1, & 0 \leq z < 100, \\ -0.1, & 100 \leq z < 300, \\ 0, & z \geq 300, \end{cases} \tag{25}$$

and $c(0) = c_0$. With the Case 4 profile there is downward refraction for the first 100 m, then upward refraction until 300 m and then a constant atmosphere. The density is set to $\rho = 1.205$ kg/m^3 and the attenuation to $2.3 \cdot 10^{-3}$ dB/km (negligible for the distances considered). The normalized surface impedance (at $z = 0$ m) is set to $\hat{Z} = 38.79 + 38.41i$.

We simulate Case 2 and Case 4 using SoundSim360 and compute the transmission loss at $z = 1$ m for both cases as follows:

$$\mathrm{TL}(r) = -20 \log_{10} \frac{p_{rms}(r)}{p_{free}}, \tag{26}$$

where $p_{rms}(r)$ is the RMS of the computed pressure field at distance r from the source and p_{free} is the RMS of the free-field pressure at 1 m distance (spherical symmetry). The upper limit of the computational domain is chosen sufficiently high to ensure it does not affect the transmission loss on the ground. In both cases, we apply our discretization method using 6th-order SBP operators with 20 grid points per wavelength (relative to 330 m/s wave speed) and a time step at 1 % of the stability limit. In Fig. 2 we plot the transmission loss up to $r = 10000$ m for both Case 2 and Case 4. Based on visual comparison, our results agree with the benchmark provided in [54].

To ensure that our reference solutions are accurate, we also simulate the problems with 10 points per wavelength and a time step at 2 % of the stability limit. We then find that the solutions are equal to approximately five decimals compared to the solutions in Fig. 2. Since the discretization is provably consistent and stable, the Lax equivalence theorem applies which guarantees convergence [55]. Hence we can conclude that the results in Fig. 2 are accurate.

5.2. Convergence study

Although the benchmark in Section 5.1 is a good test of refraction and boundary condition implementation, it does not take into account all the relevant physics for long-distance simulations. It is a two-dimensional problem in cylindrical coordinates, and it does not test 3D atmospheres or the effects of topography, for example. To further verify our method, we perform a convergence test on a 3D problem more closely related to simulations with real-world data. Unfortunately, closed-form analytical solutions to the second-order wave equation with general coefficients are difficult to derive, especially for complicated geometries. Instead, we use a synthetically generated reference solution.

Consider the domain $x, y, z \in [0, 1600] \times [0, 1600] \times [H(x, y), 800]$ m^3 presented in Fig. 3. The elevation (ground level) is given by

$$H(x, y) = H_c e^{-\frac{(x-x_c)^2}{r^2} - \frac{(y-y_c)^2}{r^2}}, \tag{27}$$

i.e., a Gaussian profile of height $H_c = 100$ m, centered at $[x_c, y_c] = [900, 700]$, with width $r = 200$ m. A point source with $f = 1$ Hz is located at $[x_s, y_s, z_s]$, where $x_s = y_s = 800$ m and $z_s = H(x_s, y_s) + 125 \approx 185.65$

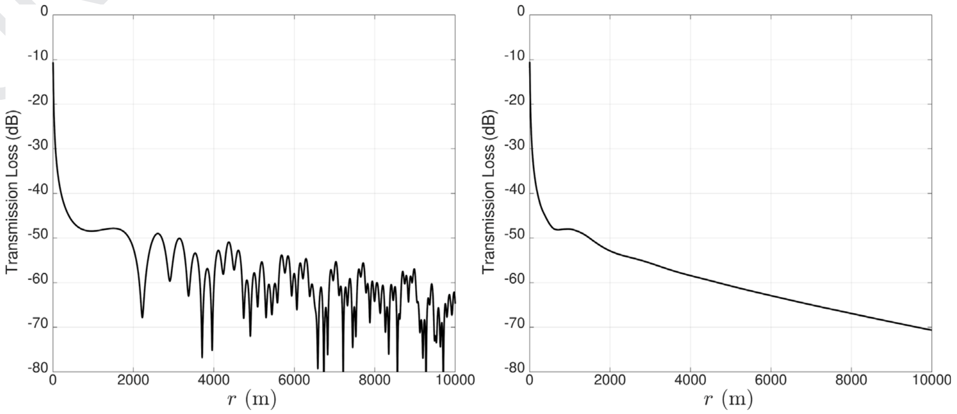

(a) Case 2

(b) Case 4

Fig. 2. Transmission loss at 1 m as a function of distance for (a) Case 2 and (b) Case 4 speed of sound profiles.

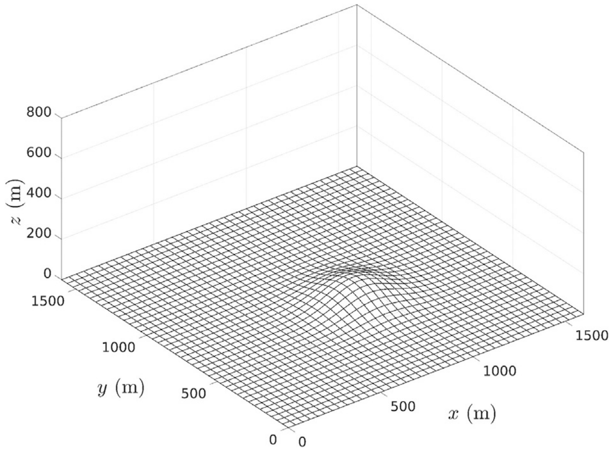

Fig. 3. Computational domain (showing only grid points at the ground).

m. The medium parameters (wave speed, density, and attenuation) are given as functions of elevation (distance from the ground), presented in Fig. 4. These profiles are derived from a typical night-time profile fitted to a fourth-degree polynomial (to guarantee smoothness).

The reference solution is obtained by simulating until $t = 1.8$ seconds using sixth-order operators on a grid with $901 \times 901 \times 451 \approx 366 \cdot 10^6$ degrees of freedom (DOF), see Fig. 5.

The time step is chosen as 1 % of the stability limit to guarantee that the temporal error is negligible. As in Section 5.1, we verify that this reference solution is sufficiently refined by comparing it to the solution on a coarser grid and find the differences small. Thus, this high-resolution reference solution can be used as a substitute for analytical solutions when comparing to less accurate approximations. Here we evaluate the convergence behavior of second and fourth-order SBP operators on grids with 3x, 6x and 10x larger spatial step sizes.

We evaluate the accuracy of the schemes in terms of the relative L_2-error, given by

$$e_p^{(N)} = \frac{||\boldsymbol{v}_p^{(N)} - \boldsymbol{v}_{ref}||_2}{||\boldsymbol{v}_{ref}||_2}, \tag{28}$$

where $\boldsymbol{v}_p^{(N)}$ is the solution of order p with N DOF and $\boldsymbol{v}_{ref}$ is the reference solution limited to the smaller grid. For two solutions with different numbers of DOF N_1 and N_2, we estimate the convergence rate as

$$q_p = \frac{\log\left(\frac{e_p^{(N_1)}}{e_p^{(N_2)}}\right)}{\log\left(\frac{N_1}{N_2}\right)^{1/3}}. \tag{29}$$

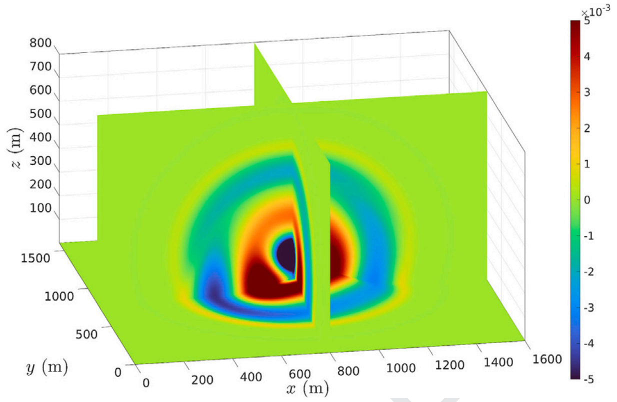

Fig. 5. The reference solution (at $t = 1.8$).

Table 1
Errors and convergence rates of second and fourth order accurate SBP operators relative to a high-resolution reference solution obtained with sixth order SBP operators.

DOF	$\log_{10}(e_2)$	q_2	$\log_{10}(e_4)$	q_4
3.8e5	−0.56	–	−0.54	–
1.7e6	−1.03	2.17	−1.01	2.16
1.4e7	−1.81	2.59	−2.23	4.07

In Table 1 the convergence rates for second and fourth-order accurate SBP operators are presented, showing that we obtain the expected convergence rates as the grid is refined.

6. Infrasound measurements

The importance of the atmosphere cannot be overemphasized when considering sound propagation, but also the sound power levels generated by modern wind turbines. There is a huge contrast between daytime and nighttime atmospheric conditions, particularly in forested regions [56] where many of the new wind farms in Sweden are located. There is also a seasonal variation in the atmospheric conditions [9], particularly over the Baltic Sea [57], affecting offshore wind farms as well as land-based wind farms.

Measuring infrasound differs fundamentally from measuring audible sound and requires carefully calibrated low-frequency instruments. The equipment used in this study is described below, in Section 6.1. Due to the large size of the source (wind turbines) and the long wavelength of 1 Hz sound (several hundred meters), receivers should not be placed

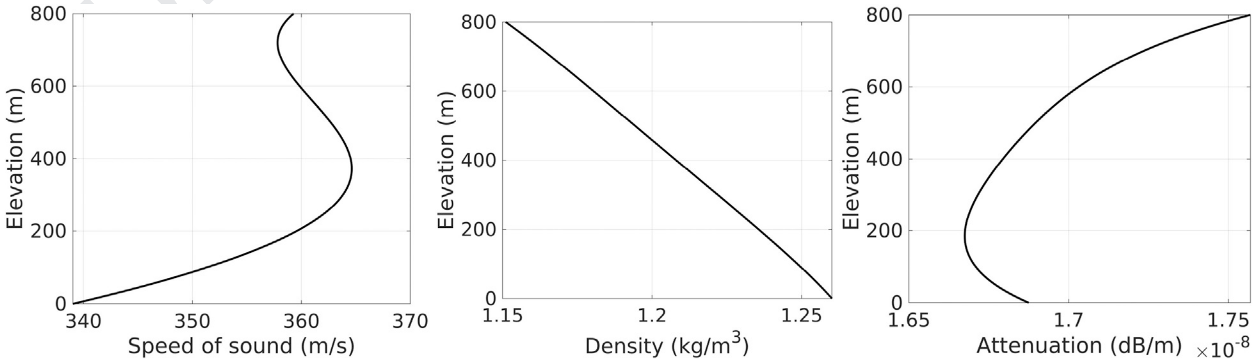

(a) (b) (c)

Fig. 4. Atmospheric data used for the convergence study: (a) speed of sound, (b) air density, and (c) acoustic attenuation.

Fig. 6. Infrasound measurement at Målarberget December 16, 2024.

in the immediate vicinity of the turbines, where the point-source approximation is less valid. Conversely, measurements should also not be taken too far away to ensure that the recorded signal originates from the wind farm of interest and to minimize modeling errors associated with atmospheric effects. Accordingly, the measurements were performed approximately 500 m to 2 km from the nearest turbine.

Table 2
The measured SPL at 1 Hz one-third octave band, Målarberget wind farm.

Measurement	Microphone 1	Microphone 2
2023–10-26 (13.00 CEST)	96.3 dB	85.6 dB
2024–10-23 (11.00 CEST)	91.6 dB	99.3 dB
2024–12-16 (12.00 CEST)	115.5 dB	–

Infrasound around 1 Hz has distinct properties compared to audible sound above 100 Hz. It is less sensitive to uncertainties in ground and atmospheric attenuation, as well as to turbulence in the atmospheric boundary layer or vegetation, due to its long wavelength. Modern wind turbines are strong emitters in this frequency range, producing levels well above typical background levels as shown in Fig. 8. These properties justify our measurement strategy and support the subsequent analysis of turbine sound power levels.

6.1. *Infrasound equipment*

Measuring infrasound down to 1 Hz accurately requires instruments that are demonstrably calibrated. A relative calibration can be carried out in a vault such as one of the CTBTO-certified infrasound stations. We performed the calibration at NORSAR relative to one of their Hyperion microphones at their station in Elverum. In the present study, a 65 mm Lidström microphone manufactured by Gargnäs Electronics in Sweden was used as a sound pressure sensor, calibrated at NORSAR. The

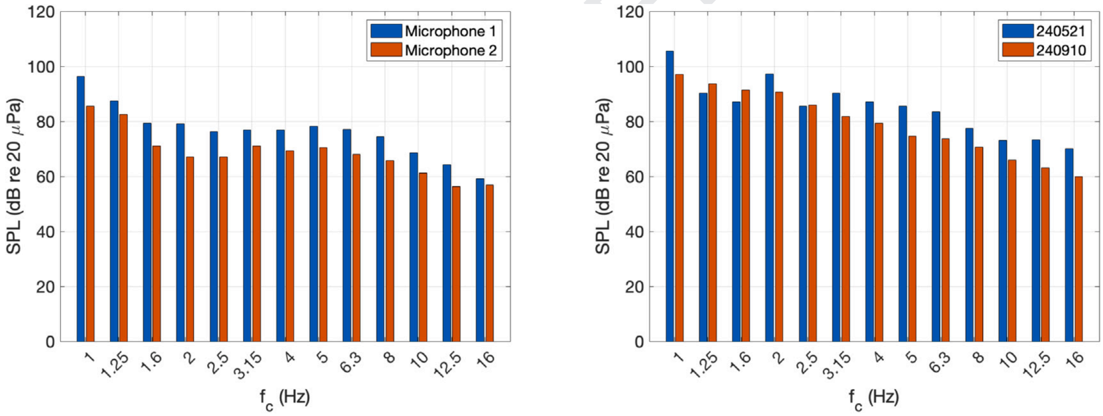

(a) Målarberget 2023-10-26 (b) Lervik 2024-05-21 and 2024-09-10

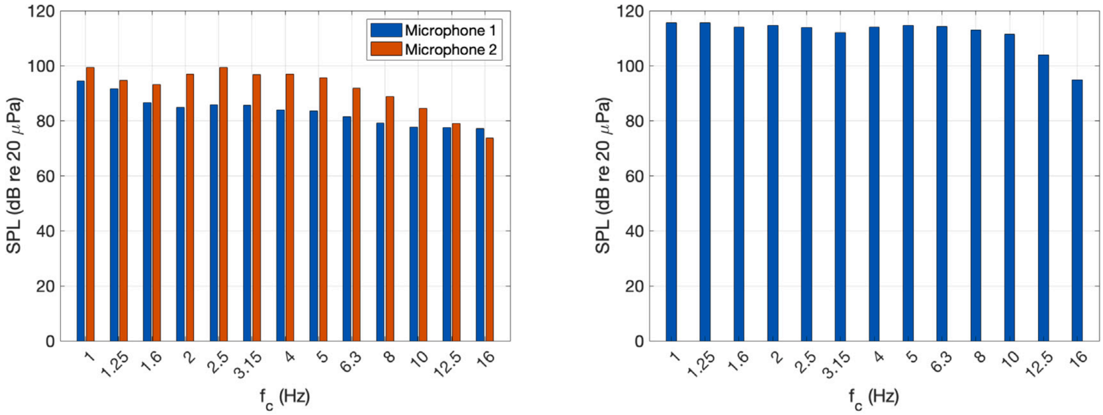

(c) Målarberget 2024-10-23 (d) Målarberget 2024-12-16

Fig. 7. Infrasound measurements (one-third octave band, center frequencies f_c 1–16 Hz) at Målarberget wind farm: (a) 2023–10-26 (13.00 CEST), (c) 2024–10-23 (11.00 CEST), (d) 2024–12-16 (12.00 CEST); and (b) Lervik 2024–05-21 (15.00 CEST), 2024–09-10 (15.00 CEST). Figs. 9–16 show the weather data.

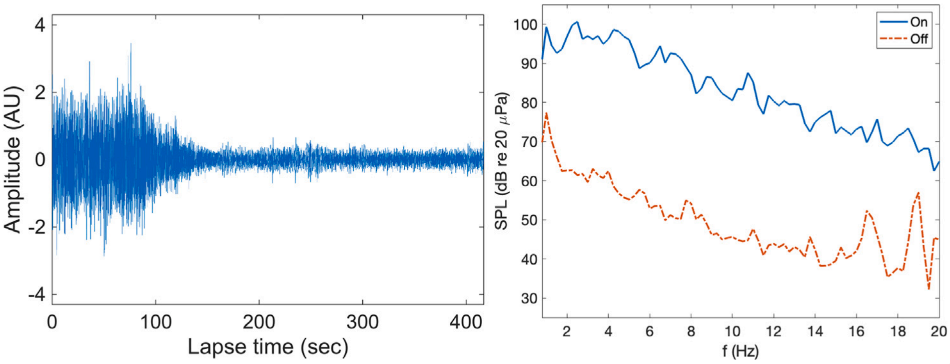

(a) Pressure fluctuations (b) Sound pressure dB

Fig. 8. (a) Time history of pressure fluctuations, (b) continuous pressure spectrum at Målarberget 2024–10-23, Microphone 2 location. With the plant On and Off. The turbine-on case is estimated from lapse time 10–60 s, while the turbine-off case is taken from lapse time 276–373 s of the time series.

Lidström microphones were developed in the early 1980s in Sweden, to detect for example helicopters. It is designed explicitly for low-frequency sound detection, and is well-suited for capturing infrasound pulses down to 1 Hz. A detailed description of the microphone's design and performance can be found in [58]. The data acquisition system was configured with a sampling frequency of 1060 Hz and, to enhance data reliability, the microphone was shielded from wind interference using a specialized metal windscreen, effectively reducing unwanted wind noise. In Fig. 6 the Lidström microphone is used to measure infrasound at Målarberget on 2024–12-16, and the results from that measurement are shown in Figs. 7 and 14. The SPL in dB is relative 20 μPa.

Remark 6. Ideally, the infrasound measurements should go down to 0.1 Hz to capture the BPF from the new larger wind turbines expected to be between 0.2–0.5 Hz. However, the Lidström microphone is only accurate down to 1 Hz. In a future project, we will use more sensitive infrasound microphones, such as Hyperion, to measure infrasound down to 0.1 Hz accurately.

6.2. Measurement results

We have conducted measurements at Målarberget wind farm three times: 2023–10-26 13.00 CEST, 2024–10-23 11.00 CEST, and 2024–12-16 12.00 CEST, and at Lervik wind farm twice: 2024–05-21 15.00 CEST and 2024–09-10 15.00 CEST. We used two microphones at different locations at Målarberget wind farm on 2023–10-26 and 2024–10-23, and one microphone on the other occasions. The locations of the measurement points in relation to the wind turbines can be seen in Figs. 12, 13, 14, 17, and 18.

Målarberget wind farm consists of 27 wind turbines of Vestas V150-4.2 MW type with a hub height of 125 m (total height is 125 + 75 = 200 m) and began operating in 2021. Lervik wind farm consists of 7 wind turbines of SG170-6.6 MW type with a hub height of 115 m (total height is 115 + 85 = 200 m) and began operating in 2024.

The results from the measurements, in terms of dB relative to 20 μPa, are shown in Fig. 7. For completeness, we show the results up to

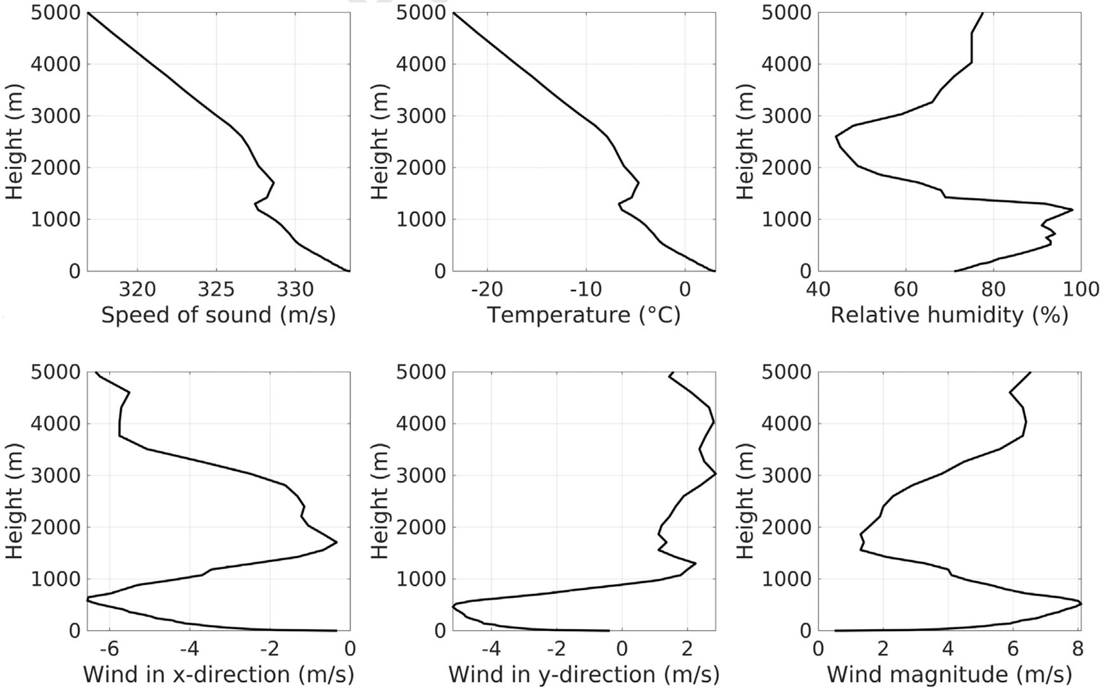

Fig. 9. Weather data (speed of sound, temperature, relative humidity and wind in x- and y-directions) in the center of Målarberget wind farm 2023–10-26 (13.00 CEST).

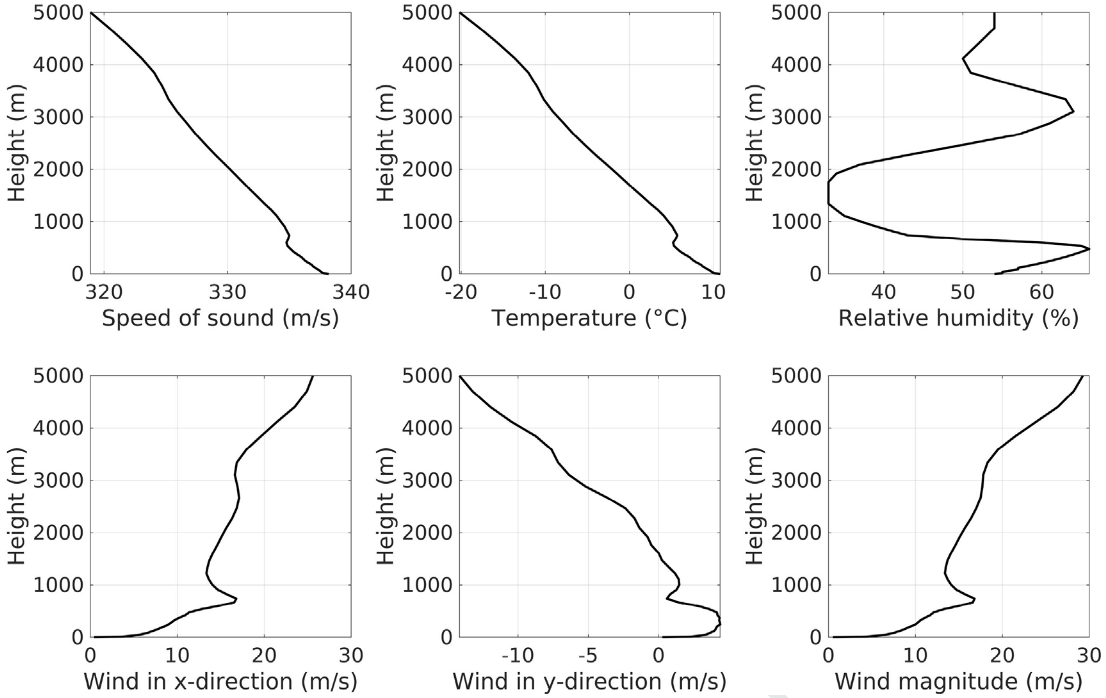

Fig. 10. Weather data (speed of sound, temperature, relative humidity and wind in x- and y-directions) in the center of Målarberget wind farm 2024–10–23 (11.00 CEST).

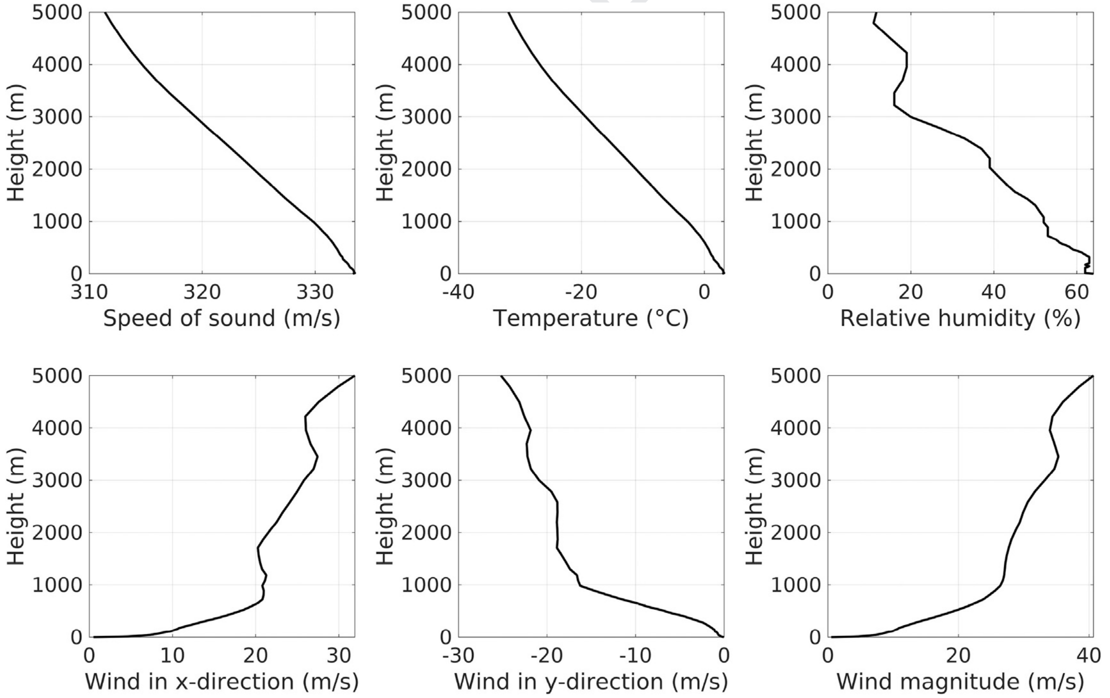

Fig. 11. Weather data (speed of sound, temperature, relative humidity and wind in x- and y-directions) in the center of Målarberget wind farm 2024–12-16 (12.00 CEST).

the 16 Hz one-third octave band, but we will focus on the 1 Hz band in the upcoming sections.

To ensure that the measured infrasound levels were not caused by background noise, we conducted continuous measurements at the Målarberget wind farm on 2024–10-23 during a complete shutdown of the facility. Fig. 8 shows the measurement data recorded at microphone position 2 on that date, capturing the period as the turbines gradually came to a stop. The recording started at 11:50 CEST and covers the transition from full operation to complete shutdown. Approximately 80 s into the measurement, the turbines began to slow down, reaching a full stop after about 150 s. During operation, the signal exhibits higher energy levels, whereas following the shutdown, the amplitude decreases rapidly and stabilizes at a substantially lower background level. These observations confirm that the increased infrasound is directly attributable to the operation of the wind turbines.

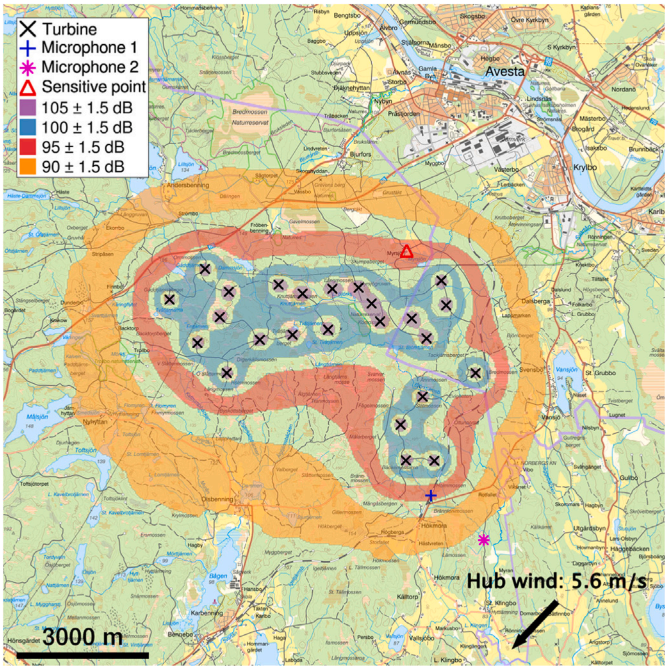

Fig. 12. Infrasound (1 Hz) simulation at Målarberget 2023–10-26 (13.00 CEST), based on two measurements (microphone 1 (96.3 dB) and microphone 2 (85.6 dB)). Here showing the simulated dB levels. The sensitive point means a nearby home (94.7 dB). Map from Lantmäteriet [59]. Weather data is presented in Fig. 9.

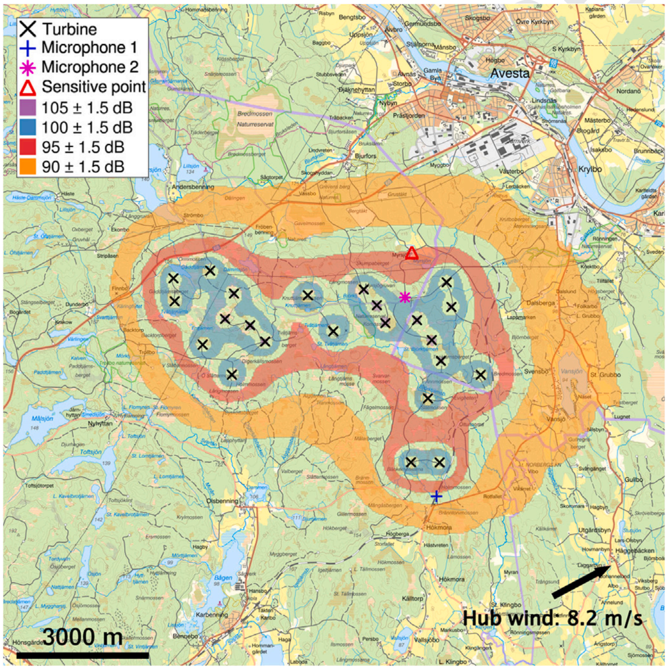

Fig. 13. Infrasound (1 Hz) simulation at Målarberget 2024–10-23 (11.00 CEST), based on two measurements (microphone 1 (91.6 dB) and microphone 2 (99.3 dB)). Here showing the simulated dB levels. The sensitive point means a nearby home (93.8). Map from Lantmäteriet [59]. Weather data is presented in Fig. 10.

7. Simulation of infrasound

The first main focus of the present study is to validate the simulation tool against accurate infrasound measurements. The second main focus is to map the sound power levels in the infrasound regime for a few modern types of wind turbines and examine the influence of the atmosphere. In the present study we will only consider the 1 Hz infrasound.

To compute the sound power levels of the wind turbines at the time of a specific measurement, we do the following:

1. Load topography and ground type data for the area of interest.
2. Load atmospheric data for the specific time of the measurement.
3. Load active turbines at the time of the measurements (often some turbines are shut down for maintenance).
4. Solve the optimization problem

$$\min_{A} \sum_{r}^{N_r} (L_{\text{meas},r} - L_{\text{tot},A}(\boldsymbol{x}_r))^2, \tag{30}$$

where N_r is the number of receiver points, $L_{\text{meas},r}$ is the measured SPL at receiver point $\boldsymbol{x}_r$, and $L_{\text{tot},A}(\boldsymbol{x}_r)$) is the total simulated SPL (defined by (10)) at receiver point $\boldsymbol{x}_r$ with amplitude A.

The sound power level in decibels is then computed from A using the standard free-field definition. Since we assume that all sources are equal, solving (30) is straightforward. Increasing the sound power levels of the

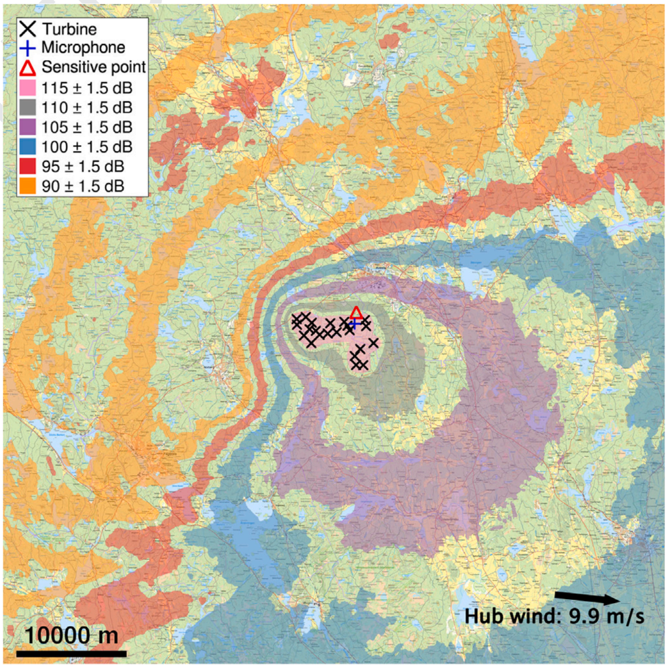

Fig. 14. Infrasound (1 Hz) simulation at Målarberget 2024–12-16 (12.00 CEST), based on measurement (115.0 dB). Here showing dB levels. The sensitive point means a nearby home (112.1 dB). Map from Lantmäteriet [59]. Weather data is presented in Fig. 11.

Table 3
The computed sound power levels and simulated SPL at 1 Hz one-third octave band, at Målarberget wind farm.

Measurement	Sound power level	Microphone 1	Microphone 2	Sensitive point
2023–10-26 (13.00 CEST)	155.0 dB	94.2 dB	87.6 dB	94.7 dB
2024–10-23 (11.00 CEST)	153.7 dB	92.8 dB	98.1 dB	93.8 dB
2024–12-16 (12.00 CEST)	172.6 dB	115.5 dB	–	112.1 dB

sources simply amounts to increasing $L_{\mathrm{tot},r}(A)$ by the same amount, thus only one simulation with each source is needed for each measurement.

7.1. Simulation of infrasound at målarberget wind farm

The measured 1 Hz SPL at the receiver points for the three separate measurements is presented in Table 2. Based on the measurements, we solve the optimization problem (30) for the sound power levels as described in Section 7 and compute (simulate) noise maps over the whole region.

A subset of the weather data we use (speed of sound, temperature, relative humidity and wind in x- and y-directions) in the center of Målarberget wind farm at the time of the measurements is shown in Figs. 9–11.

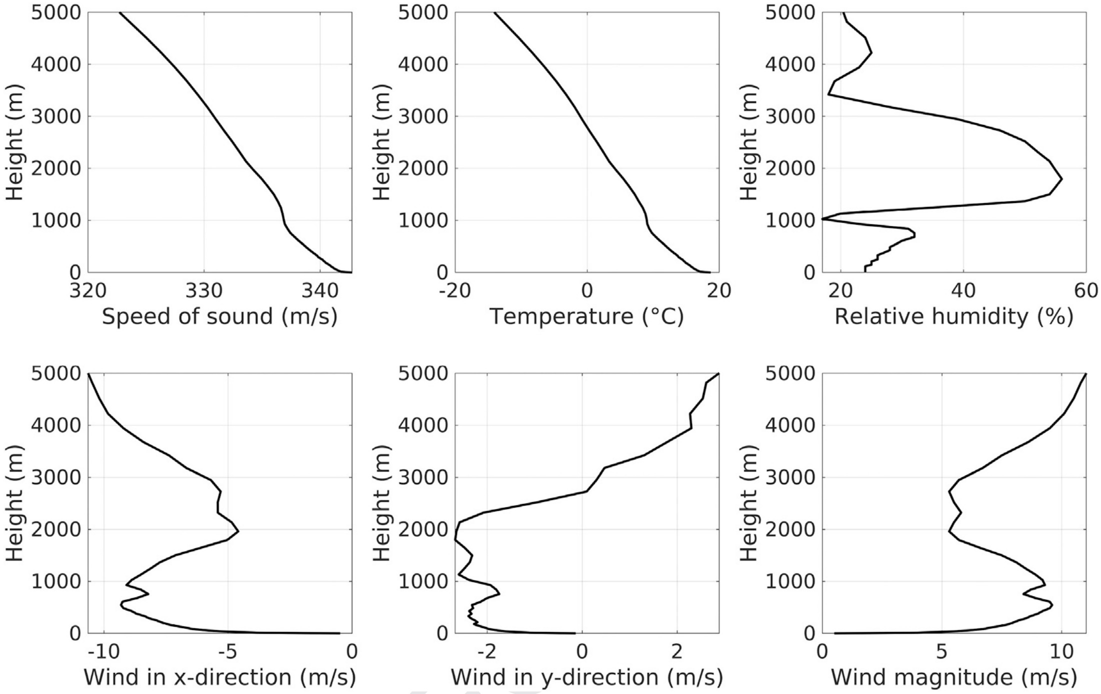

Fig. 15. Weather data (speed of sound, temperature, relative humidity and wind in x- and y-directions) in the center of Lervik wind farm 2024–05-21 (15.00 CEST).

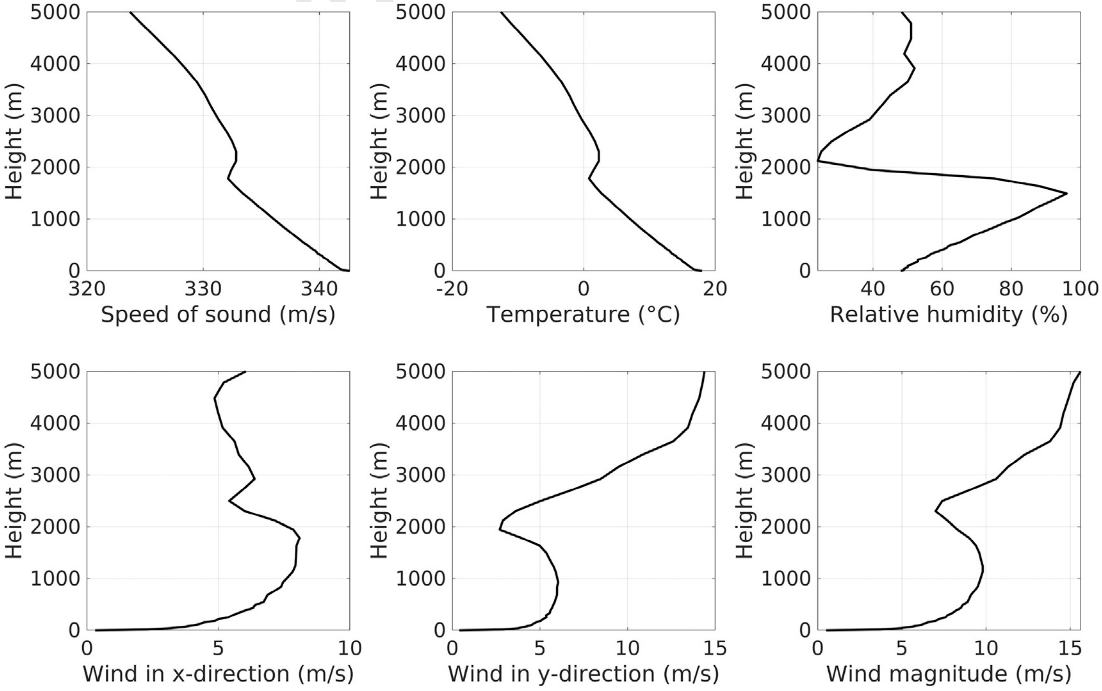

Fig. 16. Weather data (speed of sound, temperature, relative humidity and wind in x- and y-directions) in the center of Lervik wind farm 2024–09-10 (15.00 CEST).

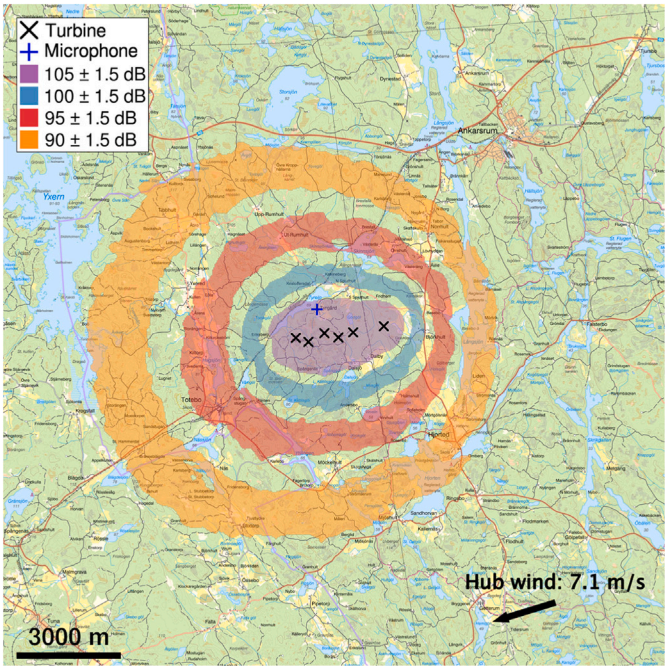

Fig. 17. Infrasound (1 Hz) simulation at Lervik 2024–05-21 (15.00 CEST), based on measurement (105.6 dB). Measurement location at a nearby home. Here showing dB levels. Map from Lantmäteriet [59]. Weather data is presented in Fig. 15.

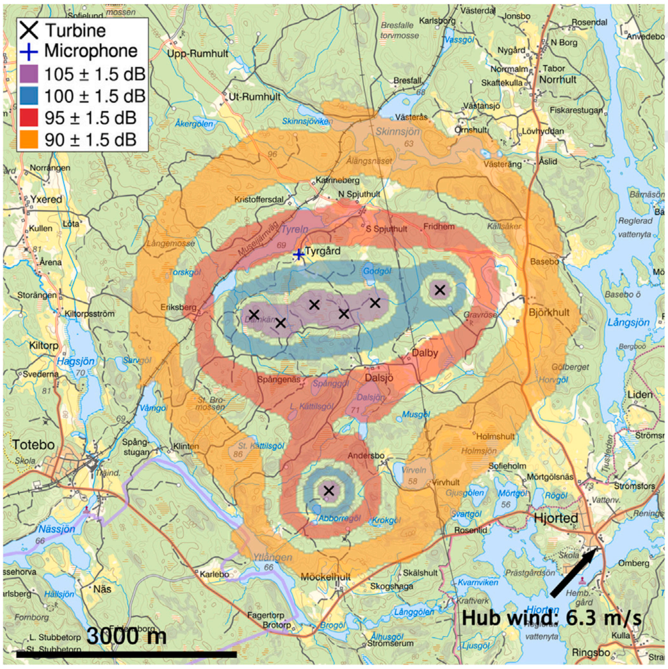

Fig. 18. Infrasound (1 Hz) simulation at Lervik 2024–09-10 (15.00 CEST), based on measurement (97.1 dB). Measurement location at a nearby home. Here showing dB levels. Map from Lantmäteriet [59]. Weather data is presented in Fig. 16.

The noise maps based on the inferred sound power levels of the sources are presented in Figs. 12, 13, and 14, one for each measurement. Note the different spatial scales in the figures. In the noise maps we have included the wind direction and strength at the hub, as well as the locations of the measurement points and a sensitive point (indicating the position of a nearby home). The computed sound power levels and simulated SPL (at the points of interest) are presented in Table 3.

Table 4
The measured SPL at 1 Hz one-third octave band, at Lervik wind farm, along with the determined wind turbine sound power levels.

Measurement	Microphone	Sound power levels
2024–05-21 (15.00 CEST)	105.6 dB	164.5 dB
2024–09-10 (15.00 CEST)	97.1 dB	156.2 dB

7.2. *Simulation of infrasound at lervik wind farm*

We perform the same procedure for the Lervik measurement data as described in Section 7.1. The weather data at the center of Lervik wind farm for the two measurements are shown in Figs. 15 and 16. The noise maps based on the inferred sound power levels are presented in Figs. 17 and 18, including the location of a nearby home (the measurement point). The SPL at 1 Hz one-third octave band at the receiver point for each measurement is presented in Table 4, along with the inferred wind turbine sound power levels determined using SoundSim360. Note that in the cases with only one receiver point, the measurements and simulations match exactly.

7.3. *Simulation of infrasound at tvinnesheda and and karskruv wind farms*

In wind farm permit applications, it is standard practice to assume a simplified atmosphere with tailwind conditions in all directions. In reality, however, the atmosphere is far from constant, and its strong influence on sound propagation (at least for audible sound) is well established. To illustrate the importance of atmospheric conditions for infrasound propagation, we use SoundSim360 to compute the SPL at 1 Hz around the Tvinnesheda and Karskruv wind farms (outside the city of Åseda, Sweden) for four different atmospheric profiles. The atmospheric parameters, given as functions of elevation, are shown in Fig. 19. Weather data were obtained on 2023–03-31, close to the spring equinox, from the center of the Målarberget wind farm: the *day* profile corresponds to 16:00 and the *night* profile to 04:00. For both the daytime and nighttime atmospheres, wind speeds were scaled to 8 m/s and 1 m/s at 10 m height, respectively, yielding four distinct atmospheric profiles.

The Tvinnesheda wind farm consists of 47 Vestas V150-4.3 MW wind turbines, and the Karskruv wind farm consists of 20 Vestas V150-4.5 MW wind turbines. Both turbine types have a hub height of 116 m and a total height of $116 + 75 = 191$ m. Tvinnesheda and Karskruv began operation in 2022 and 2023, respectively. Fig. 20 shows the simulated SPL for daytime and nighttime atmospheric profiles, with wind scaled to 1 m/s and 8 m/s at 10 m height. The sound power level (at 1 Hz) is fixed at 153.7 dB, determined from measurements conducted on 2024–10-23 at the Målarberget wind farm. Five sensitive points (A-E) corresponding to nearby residences and towns at various distances from the wind farms are included. The SPL values (1 Hz) at these points are listed in Table 5 for the four different atmospheric profiles, together with the distance to the nearest wind turbine. The results demonstrate that atmospheric conditions can significantly affect the SPL (at 1 Hz) in the far field. The largest variations occur between the daytime atmosphere with 1 m/s tailwind (at 10 m height) and the nighttime atmosphere with 8 m/s tailwind: at sensitivity point A, the difference is 3.8 dB, whereas at point E it reaches 14.5 dB.

Remark 7. Note that the measured sound power levels at the Målarberget wind farm span 153.7–172.1 dB (see Table 3). Using a sound power level of 172.1 dB instead of 153.7 dB increases the SPL at the sensitive points by 18.4 dB compared to the values listed in Table 5. The nighttime atmospheric profile, featuring an 8 m/s tailwind at 10 m height, corresponds to a highly refractive atmosphere (see Fig. 20) that induces waveguide behavior, in stark contrast to the daytime profile

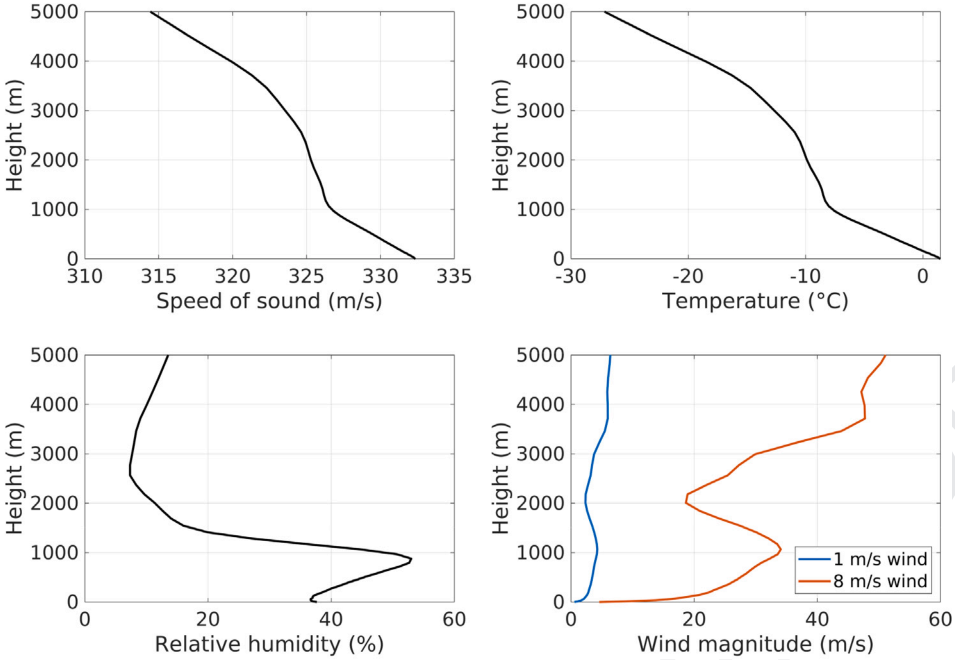

(a) Daytime

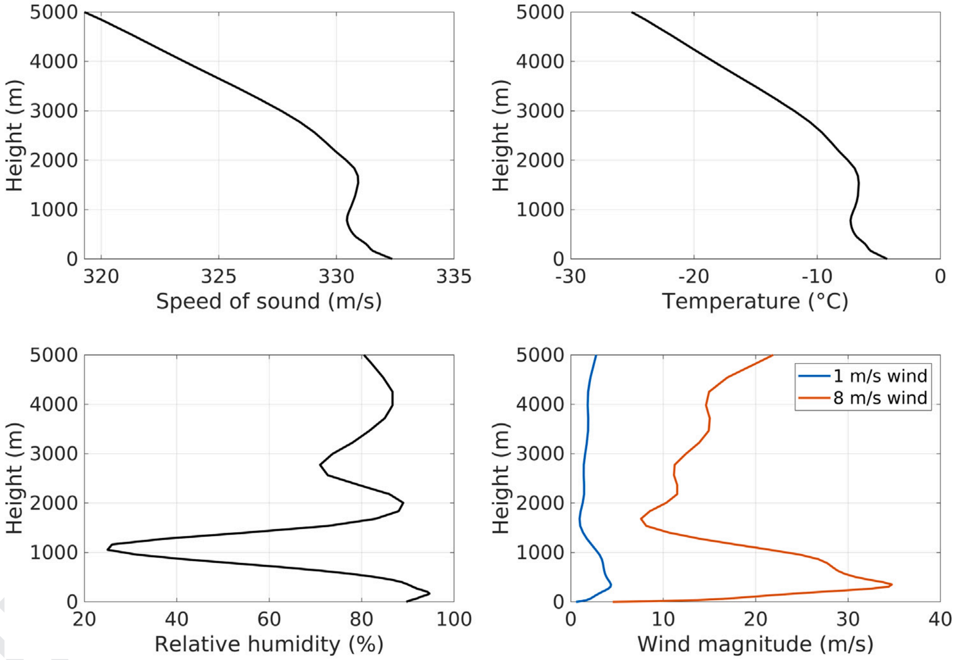

(b) Night

Fig. 19. Weather data showing the difference between (a) daytime (16.00) and (b) nighttime (04.00) March 31 2023 at the location of Målarberget wind farm. Wind speeds were scaled to 8 m/s and 1 m/s at 10 m height, respectively.

with a 1 m/s tailwind at 10 m height, which exhibits much weaker refractive effects. The daytime profile with an 8 m/s tailwind at 10 m height also induces waveguide behavior, which explains the slow decline in SPL.

8. Conclusions

We have presented a high-fidelity simulation tool for low-frequency sound propagation in large and complex three-dimensional domains. The method has been verified against benchmarks and validated with infrasound measurements from several modern wind farms, demonstrating both reliability and accuracy. The results emphasize the crucial role of realistic atmospheric data, which must be incorporated to obtain trustworthy predictions of sound propagation over long distances.

This study also shows that modern, large-scale wind turbines generate infrasound levels substantially higher than those reported for older, smaller turbines. These findings enhance the understanding of the acoustic characteristics of contemporary wind turbines and provide valuable guidance for environmental assessments and policy-making.

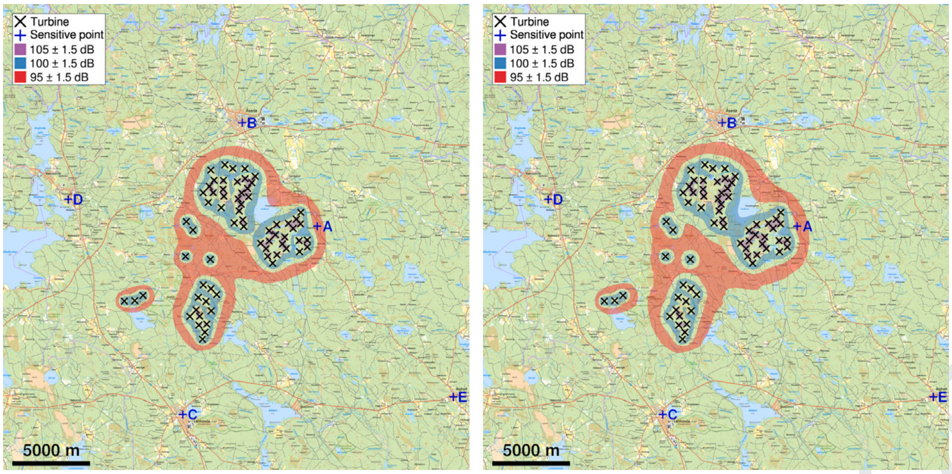

(a) Daytime atmospheric profile with 1 m/s wind. (b) Nighttime atmospheric profile with 1 m/s wind.

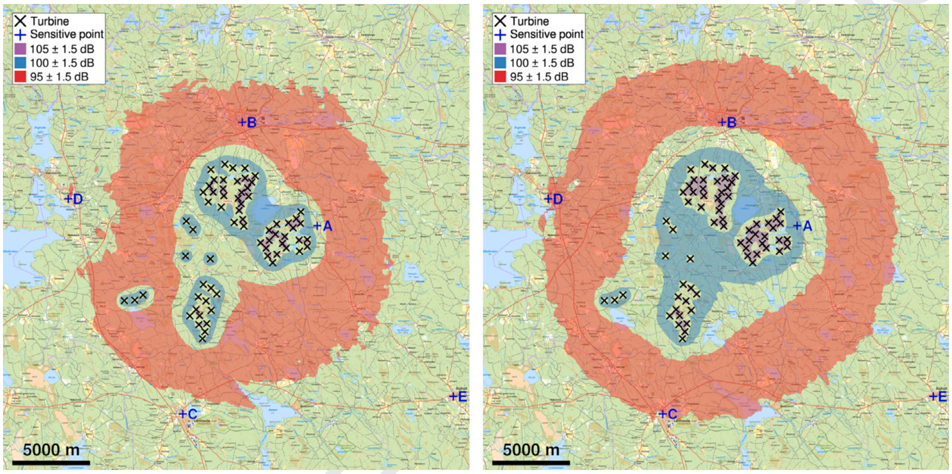

(c) Daytime atmospheric profile with 8 m/s wind. (d) Nighttime atmospheric profile with 8 m/s wind.

Fig. 20. SPL at 1 Hz around the Tvinnesheda and Karskruv wind farms under different atmospheric conditions (a)-(d). Daytime and nighttime profiles are considered, with wind scaled to 8 m/s and 1 m/s at 10 m height, respectively. SPL values at five sensitive points (A-E) near residences and towns are listed in Table 5. Maps are from Lantmäteriet [59].

Table 5
Simulated SPL at five sensitive points (A-E) around the Tvinnesheda and Karskruv wind farms for daytime and nighttime atmospheric profiles with wind speeds of 1 m/s and 8 m/s at 10 m height. Corresponding weather data are shown in Fig. 19. Distances from each point to the nearest wind turbine are included.

Atmosphere	Point A	Point B	Point C	Point D	Point E
Day profile 1 m/s	95.2 dB	88.7 dB	82.6 dB	81.2 dB	76.7 dB
Day profile 8 m/s	97.5 dB	94.6 dB	92.9 dB	93.3 dB	91.1 dB
Night profile 1 m/s	95.8 dB	90.2 dB	85.1 dB	84.1 dB	80.1 dB
Night profile 8 m/s	99.0 dB	96.3 dB	93.5 dB	93.6 dB	91.2 dB
The nearest turbine	1085 m	2924 m	5005 m	7478 m	13,460 m

Future work will focus on extending measurement capabilities using highly sensitive infrasound microphones, such as Hyperion, to capture frequencies down to 0.1 Hz, as well as investigating the directivity of wind turbine noise in the low-frequency regime.

Finally, low-frequency sound propagation in urban environments will be addressed, particularly with respect to transmission through building facades under high outdoor noise levels, which may represent a potential environmental health risk. These developments will further strengthen the applicability of SoundSim360 in environmental acoustics and its relevance for assessing potential health impacts.

CRediT authorship contribution statement

Ken Mattsson: Writing – review & editing, Writing – original draft, Validation, Supervision, Resources, Project administration, Methodology, Investigation, Funding acquisition, Formal analysis, Conceptualization. **Gustav Eriksson:** Writing – review & editing, Writing – original draft, Visualization, Validation, Software, Methodology, Investigation, Formal analysis, Conceptualization. **Leif Persson:** Writing – review & editing, Investigation, Data curation. **José Chilo:** Writing – review & editing, Resources, Investigation, Data curation. **Kourosh Tatar:** Writing – review & editing, Resources, Investigation, Data curation.

Declaration of competing interest

The authors declare the following financial interests/personal relationships which may be considered as potential competing interests:

Ken Mattsson reports that financial support was provided by Swedish Research Council. Ken Mattsson also reports that financial support was provided by Swedish Research Council Formas. Gustav Eriksson reports that financial support was provided by Swedish Research Council Formas. Gustav Eriksson also reports that financial support was provided by Swedish Research Council. If there are other authors, they declare that they have no known competing financial interests or personal relationships that could have appeared to influence the work reported in this paper.

Acknowledgements

Gustav Eriksson was supported by the Swedish Research Council (grant 2021-05830 VR) and FORMAS (grant 2022-00843). Ken Mattsson was partially supported by the Swedish Research Council (grant 2021-05830 VR), and FORMAS (grant 2022-00843).

We thank the team at NORSAR for the opportunity to perform the microphone calibration especially Jon Magnus Christensen and Tormod Kvaerna.

Data availability

Data will be made available on request.

References

[1] Recio A, Linares C, Banegas JR, Díaz J. Road traffic noise effects on cardiovascular, respiratory, and metabolic health: an integrative model of biological mechanisms. Environ Res 2016;146:359–70.

[2] Pirrera S, De Valck E, Cluydts R. Field study on the impact of nocturnal road traffic noise on sleep: the importance of in- and outdoor noise assessment, the bedroom location and nighttime noise disturbances. Sci Total Environ 2014;500: 84–90.

[3] Basner M, Babisch W, Davis A, Brink M, Clark C, Janssen S, Stansfeld S. Auditory and non-auditory effects of noise on health. The Lancet 2014;383:1325–32.

[4] Stansfeld S, Matheson M. Noise pollution: non-auditory effects on health. Br Med Bull 2003;68:243–57.

[5] Kunchur MN. The human auditory system and audio. Appl Acoust 2023;211:109507.

[6] Almquist M, Karasalo I, Mattsson K. Atmospheric sound propagation over large-scale irregular terrain. J Sci Comput 2014;61:369–97.

[7] Rydin Y, Mattsson K, Werpers J. High-fidelity sound propagation in a varying 3D atmosphere. J Sci Comput 2018;77:1278–302.

[8] Larsson C. Atmospheric absorption conditions for horizontal sound propagation. Appl Acoust 1997;50:231–45.

[9] Öhlund O, Larsson C. Meteorological effects on wind turbine sound propagation. Appl Acoust 2015;89:34–41.

[10] Pierce AD. Acoustics: an introduction to its physical principles and applications. Springer; 2019.

[11] Mattsson K, Nordström J. Summation by parts operators for finite difference approximations of second derivatives. J Comput Phys 2004;199:503–40.

[12] Mattsson K, Nordström J. High order finite difference methods for wave propagation in discontinuous media. J Comput Phys 2006;220:249–69.

[13] Mattsson K, Ham F, Iaccarino G. Stable and accurate wave-propagation in discontinuous media. J Comput Phys 2008;227:8753–67.

[14] Mattsson K, Ham F, Iaccarino G. Stable boundary treatment for the wave equation on second-order form. J Sci Comput 2009;41:366–83.

[15] Mattsson K. Summation by parts operators for finite difference approximations of second-derivatives with variable coefficients. J Sci Comput 2012;51:650–82.

[16] Stiernström V, Almquist M, Mattsson K. Boundary-optimized summation-by-parts operators for finite difference approximations of second derivatives with variable coefficients. J Comput Phys 2023;491:112376.

[17] Lantmäteriet. Terrain Model Download, grid 1+; 2021. https://www.lantmateriet.se/sv/Kartor-och-geografisk-information/geodataprodukter/produktlista/markhojdmodell-nedladdning-grid-1/.

[18] Pichon AL, Ceranna L, Vergoz J. Incorporating numerical modeling into estimates of the detection capability of the ims infrasound network. J Geophys Res Atmos 2012;117.

[19] Tope LJ, Kim JW, Spence P. Direct numerical simulations of long-range infrasound propagation: implications for source spectra estimation. J Acoust Soc Am 2024;155:465–78.

[20] Pilger C, Gaebler P, Ceranna L, Pichon AL, Vergoz J, Perttu A, Tailpied D, Taisne B. Infrasound and seismoacoustic signatures of the Sulawesi super-shear earthquake. Nat Hazards Earth Syst Sci 2019;19:2811–25 28 Sep 2018.

[21] Turquet A, Brissaud Q, Alvizuri C, Näsholm SP, Pichon AL, Kero J. Retrieving seismic source characteristics using seismic and infrasound data: the 2020 ml 4.1 kiruna minequake, Sweden. Geophys Res Lett 2024;51.

[22] Toney L, Fee D, Schmandt B, Bishop JW. Examining infrasound propagation at high spatial resolution using a nodal seismic array. J Geophys Res Solid Earth 2023;128.

[23] Blixt EM, Näsholm SP, Gibbons SJ, Evers LG, Charlton-Perez AJ, Orsolini YJ, Kvaerna T. Estimating tropospheric and stratospheric winds using infrasound from explosions. J Acoust Soc Am 2019;146:973–82.

[24] Wilson DK, Shaw MJ, Ostashev VE, Muhlestein MB, Alter RE, Swearingen ME, McComas SL. Numerical modeling of mesoscale infrasound propagation in the arctica. J Acoust Soc Am 2022;151:138–57.

[25] Hupe P, Pilger C, Pichon AL, Ceranna L. Probing atmospheric waves and the middle atmosphere dynamics using infrasound. J Acoust Soc Am 2024;155:A201.

[26] Ambrose SE, Rand RW, Krogh CME. Wind turbine acoustic investigation: infrasound and low-frequency noise – a case study. Bull Sci Technol Soc 2012;32:128–41.

[27] Salt AN, Hullar TE. Responses of the ear to low frequency sounds, infrasound and wind turbines. Hear Res 2010;268:12–21.

[28] Salt AN, Kaltenbach JA. Infrasound from wind turbines could affect humans. Bull Sci Technol Soc 2011;31:296–302.

[29] Salt AN, Lichtenhan JT. How does wind turbine noise affect people. Acoust. Today 2014;10:20–8.

[30] Pluess M, Assary E, Lionetti F, Lester KJ, Krapohl E, Aron EN, Aron A. Environmental sensitivity in children: development of the highly sensitive child scale and identification of sensitivity groups. Translational Psychiatry 2018;54:51–70.

[31] Lionetti F, Aron A, Aron EN, Burns GL, Jagiellowicz J, Pluess M. Dandelions, tulips and orchids: evidence for the existence of low-sensitive, medium-sensitive and high-sensitive individuals. Transl Psychiatry 2018;8:24.

[32] Weichenberger M, Bauer M, Kühler R, Hensel J, Forlim CG, Ihlenfeld A, Ittermann B, Gallinat J, Koch C, Kühn S. Altered cortical and subcortical connectivity due to infrasound administered near the hearing threshold - evidence from fmri. PLoS One 2017;12:1–19.

[33] Forlim CG, Ascone L, Koch C, Kühn S. Resting state network changes induced by experimental inaudible infrasound exposure and associations with self-reported noise sensitivity and annoyance. Scientific Reports 2024;14:24555.

[34] Danielsson AA, Landström U. Blood pressure changes in man during infrasonic exposure. Acta Med Scand 1985;217:531–5.

[35] Tolvanen A, Routavaara H, Jokikokko M, Rana P. How far are birds, bats, and terrestrial mammals displaced from onshore wind power development? – a systematic review. Biol Conserv 2023;288:110382.

[36] Marshall NS, Cho G, Toelle BG, Tonin R, Bartlett DJ, Rozario ALD, Evans CA, Cowie CT, Janev O, Whitfeld CR, Glozier N, Walker BE, Killick R, Welgampola MS, Phillips CL, Marks GB, Grunstein RR. The health effects of 72 hours of simulated wind turbine infrasound: a double-blind randomized crossover study in noise-sensitive, healthy adults. Environ Health Perspect 2023;131:037012.

[37] Maijala PP, Kurki I, Vainio L, Pakarinen S, Kuuramo C, Lukander K, Virkkala J, Tiippana K, Stickler EA, Sainio M. Annoyance, perception, and physiological effects of wind turbine infrasound. J Acoust Soc Am 2021;149:2238–48.

[38] Schäffer B, Pieren R, Schlittmeier SJ, Brink M. Effects of different spectral shapes and amplitude modulation of broadband noise on annoyance reactions in a controlled listening experiment. Int J Environ Res Public Health 2018;15.

[39] Virjonen P, Hongisto V, Radun J. Annoyance penalty of periodically amplitude-modulated wide-band sound. J Acoust Soc Am 2019;146:4159–70.

[40] Kelley ND, McKenna HE, Hemphill RR, Etter CL, Garrelts RL, Linn NC. Acoustic noise associated with the MOD-1 wind turbine: its source, impact, and control, technical report, solar energy research Inst. (SERI) 1985, Golden, CO (United States).

[41] Parakkal S, Gilbert KE, Di X, Bass HE. A generalized polar coordinate method for sound propagation over large-scale irregular terrain. J Acoust Soc Am 2010;128:2573–80.

[42] Attenborough K. Acoustical impedance models for outdoor ground surfaces. J Sound Vib 1985;99:521–44.

[43] Ostashev V, Wilson D. Acoustics in moving inhomogeneous media. CRC Press; 2015.

[44] Salomons E. Computational Atmospheric Acoustics. Dordrecht: Kluwer Academic Publishers; 2001.

[45] Hornikx M, Dohmen M, Conen K, van Hooff T, Blocken B. The wind effect on sound propagation over urban areas: predictions for generic urban sections. Build Environ 2018;144:519–31.

[46] I.O. for Standardization, Acoustics: Attenuation of Sound During Propagation Outdoors 1993, International Organization for Standardization.

[47] Ostashev VE, Wilson DK. Acoustics in moving inhomogeneous media. J Acoust Soc Am 1999;105:2067.

[48] Naturvårdsverket. Nationella marktäckedata (NMD) 2023/2018 – produktbeskrivning, utgåva 1.1; 2025. https://www.naturvardsverket.se/verktyg-och-tjanster/kartor-och-karttjanster/nationella-marktackedata/.

[49] Gustafsson B, Kreiss H-O, Oliger J. Time-dependent problems and difference methods. 2013, 2.

[50] Virta K, Mattsson K. Acoustic wave propagation in complicated geometries and heterogeneous media. J Sci Comput 2014;61:90–118.

[51] Petersson NA, O'Reilly O, Sjögreen B, Bydlon S. Discretizing singular point sources in hyperbolic wave propagation problems. J Comput Phys 2016;321:532–55.

[52] Almquist M, Dunham EM. Non-stiff boundary and interface penalties for narrow-stencil finite difference approximations of the laplacian on curvilinear multiblock grids. J Comput Phys 2020;408:109294.

[53] Svärd M, Nordström J. On the convergence rates of energy-stable finite-difference schemes. J Comput Phys 2019;397:108819.

[54] Attenborough K, Taherzadeh S, Bass HE, Di X, Raspet R, Becker GR, Güdesen A, Chrestman A, Daigle GA, L'Espérance A, Gabillet Y, Gilbert KE, Li YL, White MJ, Naz P, Noble JM, van Hoof HAJM. Benchmark cases for outdoor sound propagation models. J Acoust Soc Am 1995;97:173–91.

[55] Lax P, Richtmyer R. Survey of the stability of linear finite difference equations. Commun Pure Appl Math 1956;IX:267–93.

[56] Arnqvist J, Olivares-Espinosa H, Carlén I. Wind energy relevant characteristics of turbulence over boreal forests, In: Journal of Physics: Conference Series 2767; (2024) 092096.

[57] Hallgren C, Arnqvist J, Nilsson E, Ivanell S, Shapkalijevski M, Thomasson A, Pettersson H, Sahlée E. Classification and properties of non-idealized coastal wind profiles – an observational study. Wind Energy Sci 2022;7:1183–207.

[58] Liszka L. Infrasound: a summary of 35 years of infrasound research, irf scientific report. Swedish Institute of Space Physics; 2008.

[59] Lantmäteriet, Map 1:(50) 000, raster, 2018, https://www.lantmateriet.se/sv/geodata/vara-produkter/produktlista/karta-150-000-nedladdning-raster/.